A&A 425, 187–206 (2004)
DOI: 10.1051/0004-6361:20040421

Astronomy & Astrophysics

Subgiants as probes of galactic chemical evolution⋆,⋆⋆,⋆⋆⋆

P. Thorén, B. Edvardsson, and B. Gustafsson

Department of Astronomy and Space Physics, Uppsala Astronomical Observatory, Box 515, 751 20 Uppsala, Sweden
e-mail: bengt.edvardsson@astro.uu.se

Received 10 March 2004 / Accepted 28 May 2004

Abstract. Chemical abundances for 23 candidate subgiant stars have been derived with the aim at exploring their usefulness for studies of galactic chemical evolution. High-resolution spectra from ESO CAT-CES and NOT-SOFIN covered 16 different spectral regions in the visible part of the spectrum. Some 200 different atomic and molecular spectral lines have been used for abundance analysis of ∼30 elemental species. The wings of strong, pressure-broadened metal lines were used for determination of stellar surface gravities, which have been compared with gravities derived from Hipparcos parallaxes and isochronic masses. Stellar space velocities have been derived from Hipparcos and Simbad data, and ages and masses were derived with recent isochrones. Only 12 of the stars turned out to be subgiants, i.e. on the "horizontal" part of the evolutionary track between the dwarf- and the giant stages. The abundances derived for the subgiants correspond closely to those of dwarf stars. With the possible exceptions of lithium and carbon we find that subgiant stars show no "chemical" traces of post-main-sequence evolution and that they are therefore very useful targets for studies of galactic chemical evolution.

Key words. stars: abundances – stars: evolution

1. Introduction

Abundance patterns in stellar populations have proven to be a powerful means of studying galactic chemical evolution and nucleosynthesis. Studies like Edvardsson et al. (1993, EAGLNT), Feltzing & Gustafsson (1998), Chen et al. (2000) and Fuhrmann (2004) show that with a large number of stars the history of the chemical elements can be mapped to disclose essentials of the star formation history at different locations in the Galaxy.

Even with the impressive amount of data presented in the papers mentioned above only a tiny sphere with radius some 100 pc around the Solar system has been explored with the high accuracy achievable from dwarf-star spectra. Knowledge of stellar kinematics enable extension of this sphere, but only regions within 2 kpc of the solar galactocentric radius have been systematically probed by these stars. Compared to the dimensions of the Galaxy, this is certainly a small region. The generalization of results gained from studying stars that currently neighbour the Solar system will very likely be locally biased.

The volume is limited by the low luminosities of the dwarfs used in the surveys, and by the limited view in certain directions through the galactic disk. Subgiants are 1–2 mag brighter than dwarfs, which opens up larger volumes for study. With the use of VLT-sized telescopes, subgiant targets increase the observable radius from the Earth by more than ten times, and e.g. allow studies of the thick galactic disk where it dominates the stellar number density. Subgiant stars are, due to their relatively rapid evolution, much more rare than dwarfs. However, with a volume increased >1000 times there will be enough objects available for detailed chemical-evolution studies. The problem with reddening will become more important for distant subgiants. Therefore, future investigations must use methods designed for estimating stellar parameters regardless of reddening or independent determination of reddening, unless dust-free windows in the disk can be used. For important studies of halo and disk stars close to the Galactic pole the reddening problem is reduced.

The subgiant stars, although recognised as a specific stellar group by 1930 (Strömberg 1930), were not understood in terms of stellar evolution until the 1950ies. At the Vatican Conference on Stellar Populations in 1957, it was first realised that the use of these stars offered possibilities for dating the Galactic disk (see references in the interesting review of the history of subgiants by Sandage et al. 2003). The facts that the isochrones separate nicely for different ages in the subgiant region, and that they run almost horizontally in the $T_{\rm eff} - M_{\rm bol}$ diagram, make the stars particularly suitable for dating purposes. This requires, however, a good determination of $M_{\rm bol}$, i.e. the stellar parallaxes, or of the surface gravity.

In this work, based on high resolution spectroscopy data, we explore the use of subgiants for studies of galactic chemical evolution by investigating a sample of nearby subgiants and comparing the resulting abundances with those of more

⋆ Based on observations made at ESO, La Silla.
⋆⋆ Based on observations made at NOT, La Palma.
⋆⋆⋆ Tables 1 and 2 are only available in electronic form at http://www.edpsciences.org

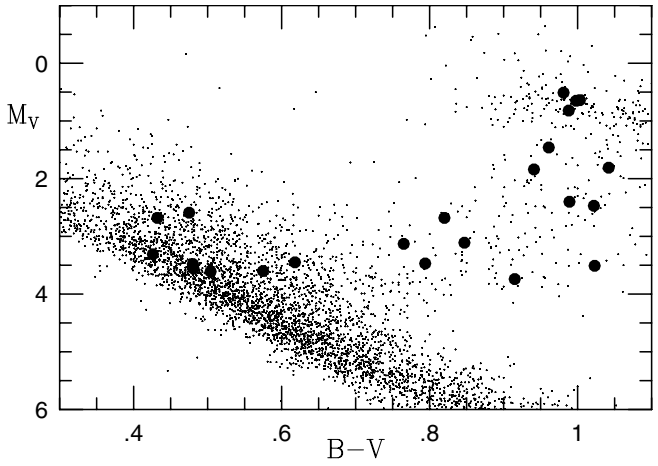

Fig. 1. The positions of our programme stars (large circles) in an observational HR diagram compared to Hipparcos stars with relative parallax errors of 5% or less.

unevolved dwarf stars. We will conclude that they may represent the best suited stellar group for this kind of study.

In Sects. 2–5 the observations, data reductions and spectrum analysis are described. In Sects. 6 and 7 the ages, masses and dynamical properties of the stars are derived, while Sect. 8 discusses different sources of errors in the analysis. Section 9 presents the abundance results, and finally Sects. 10 and 11 give a discussion of the results and the conclusions of this work.

2. Observations and reductions

To find a test sample of *bona fide* subgiant stars with a range of metallicities the compilation of [Fe/H] determinations of Cayrel de Strobel et al. (1997) was used. Stars with luminosity class IV and $\log g$ values around 3.0 (cgs) were found, and a number of objects with different metallicities were chosen for possible observation. At that time, the Hipparcos (ESA 1997) data was unfortunately not yet available. After the release of these data several of our target stars turned out not to be subgiants as shown by the colour-magnitude diagram in Fig. 1. During the course of the analysis three stars were also found to be Pop. II giants, HD 4306, HD 44007, and HD 128279. These stars were excluded from the discussion in the present paper.

The observational data were obtained during three observation runs in 1997. The ESO CAT-CES at La Silla, Chile, was used in the periods March–April (eight nights) and October–November (eight nights). The NOT-SOFIN at La Palma was used in October–November (eight nights). The observations at La Silla were made without problems. Four nights of eight at NOT were useless due to bad weather and the great '97 vegetation fire that lasted for one full night.

The spectra were reduced with the MIDAS software and routines. The CES spectra consist of one echelle order only, and were reduced with the MIDAS LONG context. The SOFIN spectra have several orders. These were extracted with the MIDAS ECHELLE context.

With the single-order CES the wavelength settings were changed several times each night. For every new setting during the observations a Th-Ar exposure was taken, which was used for the wavelength calibration.

Scattered light background components were removed from the exposures by subtracting a constant, where needed, for the CAT spectra, and by the ECHELLE background fitting function for the NOT multi-order echelle spectra.

3. Stellar parameters

Object selection and initial stellar parameter values were based on the Cayrel de Strobel et al. (1997) compilation. which contains published data from hundreds of sources. The stellar parameters had been derived by different authors and some stars lacked a complete set of parameters. Median values were used for objects with several parameter determinations. During the autumn 1997 runs the Hipparcos (ESA 1997) catalogue had been released and subgiants could also be picked from there. The latter catalogue does however not provide stellar parameters. Literature search during the analysis provided scattered data where, again, median values were used for reasonably modern parameter determinations. The atmospheric model parameters (except $T_{\rm eff}$) were modified during the course of the analysis. Surface gravities were determined from the wings of strong lines (see Sect. 5) and the metallicity from the [Fe/H] abundance. Since late-type giant-star atmospheres may be out of LTE excitation balance for low excited Fe lines (Allende Prieto et al. 1999; Steenbock 1985), these lines could not be used to determine the effective temperature (e.g., Thorén 2000). Therefore literature values for $T_{\rm eff}$ were used through the whole analysis and furthermore the Fe abundance was determined by the use of highly excited lines only ($\chi > 3.5$ eV).

4. Model atmospheres and abundance analysis

4.1. Model atmospheres

A version (Asplund et al. 1997) of the LTE, plane-parallel, flux constant MARCS atmospheres (Gustafsson et al. 1975) were used to represent the atmospheres of the observed stars.

4.2. Analysis codes

The Uppsala analysis codes SPECTRUM and EQWIDTH were used for the abundance derivation. SPECTRUM was used to fit synthetic spectra to observed ones. The equivalent widths of the lines fitted were analysed with EQWIDTH, which yields mean values and scatter of abundances from measured equivalent widths.

4.3. Atomic and ionic lines

Basic atomic line data was fetched from the VALD database (Piskunov et al. 1995). The intention of our work was to make a differential analysis relative to the Sun; consequently we fitted the oscillator strengths of the lines to match the strength of the solar flux spectra that were taken during the observational runs. The VALD oscillator strengths usually agree within one order of magnitude with the astrophysical oscillator strengths.

For some lines the solar lines were too weak to enable a reliable value of the oscillator strength. In these cases values from the literature were used. The adopted atomic line data is given in Table 1 (available in electronic form only) which gives the wavelength, $\log gf$ value, excitation energy, and damping parameters for each of the 159 lines of atoms and first ions with wavelengths between 4388 and 8758 Å. The species are identified in Table 6, Sect. 9.

A flux-constant solar model may not be ideal for determination of oscillator strengths. The present work is a differential study which means that most errors in the atomic data will hopefully cancel out when data of solar-like stars are interpreted. Most stars in this sample are not dwarf-like, rather they are subgiants and giants. The effect of errors in the astrophysical $\log gf$ values would therefore be expected to show up as small but systematic shifts in the derived abundances. The shape of these patterns are, however, not expected to change very much due to these errors.

Pressure broadening data for the lines was based on quantum mechanical calculations by Barklem & O'Mara (1998, and references therein). For many lines, particularly ionic lines, such data are not available. In those cases the classical Unsöld damping constant was assumed and multiplied by a factor typical for the element. These factors are listed in Table 1 (available in electronic form only). For the Cu I line at 5105.5 Å, hyperfine structure splitting was considered and the solar isotopic ratio ^{63}Cu/^{65}Cu = 0.69/0.31 was assumed for all stars.

First, all stars were analysed by means of synthetic spectroscopy in the regions centered at 4383, 5269 and 6162 Å. The results from these regions gave new values for metallicity (Fe abundance), surface gravities (pressure broadening of strong lines) and microturbulence parameters (balance in abundances from strong/weak Ca, Fe and Ni lines). The remaining regions were analysed with atmospheric models based on these parameters.

During the analysis up to 200 different atomic, ionic and molecular features were analysed, and in many cases dropped if close inspection showed that they are blended by unknown lines (e.g., in the solar spectrum or exposed when a particular line gives deviating abundances for atmospheres with low $T_{\rm eff}$).

4.4. Molecular lines

Absorption features from CH, C_2, CN, ^{13}CN and MgH present in our wavelength regions were used for abundance determinations of carbon, nitrogen and magnesium. Molecular lines were detected in most of our programme stars except for the hottest ones. The "molecular" abundances are presented separately from those determined from atomic and ionic lines to enable discussion of the internal consistency in the analysis. Line data for the most important molecular features; wavelengths, excitation energies and oscillator strengths, are given in Table 2 (only available in electronic form).

Adopting the oxygen abundances from Sect. 9.4, carbon abundances were found from CH and C_2 lines, and nitrogen abundances were derived from CN lines. For stars without spectra of oxygen lines, we adopted oxygen abundances typical for stars of EAGLNT with similar [Fe/H].

Basic data for ^{12}CH A–X (0, 0) and (1, 1) lines in the wavelength regions $\lambda\lambda$ 4180–4220 and 4285–4315 were adopted from Jørgensen et al. (1996). Features of the A–X (1, 1) band were shifted to the solar wavelengths reported by Moore et al. (1966), and all gf values were decreased by 0.12 dex. This shift would not have been necessary if the semiempirical solar model of Holweger-Müller (1974) had been adopted. For consistency reasons we here use a MARCS theoretical model also for the Sun, hoping that possible model deficiences will cancel out to some degree in a relative abundance analysis. A maximum of 22 useful CH features were used for each star and the line-to-line abundance scatter was typically 0.05 dex (ranging between 0.03 to 0.10).

^{12}C^{12}C A–X (0, 0) line data in the 5085–5165 Å region was adopted from Querci et al. (1971). The wavelengths of the dominating lines were modified to fit our solar observations and the solar flux atlas of Kurucz et al. (1984). No modification of the gf values was found to be necessary. Carbon abundances for 17 stars were derived from typically 3, but depending on the observed wavelength regions up to 7, C_2 features that were judged to be negligibly contaminated by other lines. The line-to line abundance scatter was typically 0.03 dex (0.00 to 0.09).

Violet and red ^{12}C^{14}N line data in the 4180–4215 (B–X (0, 1) and (1, 2)) and 7980–8020 Å (A–X (2, 0)) regions were adopted from Plez (2001), with the experimental CN dissociation energy of 7.77 eV of Costes et al. (1990). The CN line wavelengths were found to give a very good agreement with the solar spectrum. In the 4200 Å region the oscillator strengths had to be decreased by 0.12 dex, just like for the CH lines in the same region discussed above. In the red region the solar spectrum was very well fit without any modifications to the CN line data. Nitrogen abundances were derived from up to 25 lines in the violet region, with line-to-line scatter of typically 0.06 dex. In the red region up to 8 lines could be used with a similar line-to-line scatter.

In the 7920–8020 Å region 10–20 red ^{13}C^{14}N A–X (2, 0) features could be identified and used for determinations of ^{12}C/^{13}C isotope ratios from the observations of 6 stars. This measurement is insensitive to uncertainties in the abundances of C, N (and O) since only the relative strengths of the ^{12}CN and ^{13}CN features enter. Line data from Plez (2001) were adopted, and for the about 100 strongest lines laboratory wavelengths were found in Wyller (1966) and adopted. Wavelength corrections of +0.1 to +0.4 Å were typically needed to Plez's data. The strongest ^{13}CN feature in the region falls at 8004.3–8004.7 Å and this was the main criterion for the isotopic ratio, with consideration also of the weaker features. The uncertainties were conservatively assumed as the standard deviation (scatter) of the various ^{13}CN features used in each spectrum. The resulting ^{12}C/^{13}C ratios are presented in Table 6. Spectra for another six stars were obtained for the 7970 Å region. Four of these were too hot to show any CN lines (HDs 400, 61421, 207978 and 212487), and those for the other two (HDs 6734 and 24616) ended bluewards of the 8004 Å ^{13}CN feature.

Table 3. Surface gravities from different lines and methods. The parallax 0.″045 was adopted for HD 82734 (van Altena & Hoffleit 1996). Fe (ion bal.) shows gravities assuming LTE ionisation balance for Fe. The column marked "Adopted" shows the surface gravities used for the abundance determination.

Star	Mg I 5167	Mg I 5172	Ca I 6162	Fe I 4383	Fe I 5269	Fe ion bal.	Hipparcos from π	Adopted
HD 400	4.13	3.98		4.15		3.85	4.07	3.98
HD 2151	3.78	3.70	4.08		3.83	3.87	3.95	3.93
HD 6734	3.70	3.70	3.40		3.55	3.28	3.47	3.40
HD 18907	4.31	4.31	4.01		4.01	3.90	3.86	4.21
HD 22484	4.00	4.00	3.96		4.12	3.92	4.09	3.96
HD 23249	3.65	3.60					3.67	3.82
HD 24616	3.50	3.30	3.10		3.10	3.33	3.22	3.10
HD 35410	3.00	2.86	3.16		3.10	2.85	3.01	3.16
HD 40409		3.40	3.30		3.30	2.62	3.12	3.30
HD 61421	4.30	4.15				3.80	4.02	4.02
HD 62644	3.50	3.42	3.50		3.75	3.27	3.65	3.42
HD 82734			3.25			2.33		3.11
HD 111028			3.10		3.10	2.55	3.03	3.10
HD 115577	2.90	2.75	2.75		2.65	2.45	2.30	2.75
HD 130952	2.45	2.28	2.18		2.43	1.50	2.43	2.43
HD 142198	2.76	2.61	3.11			2.25	2.57	2.91
HD 168723	3.30	3.10	2.95		2.95	2.87	3.01	2.95
HD 196171	2.70	2.60	3.00			2.10	2.63	3.00
HD 197964	3.10	2.95	3.25		3.25	2.75	3.10	3.25
HD 199623	3.97	3.97	4.27			3.95	4.13	4.27
HD 207978	4.05	3.90		4.05		3.90	4.04	3.90
HD 212487	3.75	3.75		3.60		3.60	3.83	3.60
HD 219617	4.10	4.05		3.90		3.90	3.83	3.90

MgH A–X (0, 0) line data for the region 5140–5195 Å was adopted from Kurucz (1994). Wavelengths and gf values were then individually modified to fit our solar observations and the solar flux atlas of Kurucz et al. (1984). For 9 stars our spectra enabled abundance determinations from typically 7 MgH lines, with line-to-line scatters of typically 0.10 dex. The derived magnesium abundances are not sensitive to the C, N, O element abundances within their uncertainties.

5. Surface gravities

The purpose of this investigation is to study how useful subgiants may be for chemical evolution studies. The luminosity class alone is usually not sufficient to identify such objects, $\log g$ is also needed. Spectroscopic determination of surface gravity is a powerful distance-independent method to sort out subgiants from giants or dwarfs. Another method is by the use of accurate parallaxes.

5.1. Spectroscopy

Pressure-broadened lines are sensitive to surface gravity and we use the wings of such lines to derive $\log g$ (Blackwell & Willis 1977; Edvardsson 1988). Ideally, to compensate for uncertainties in the model atmospheric parameters and possible deviations from LTE, the abundances used in the calculation of the strong line should be derived from weak lines with the same lower energy level.

Depending on the stellar metallicity, we observed some of the spectral regions containing the following strong and pressure-broadened metal lines: Fe I 4383.6 and 5269.5 Å, Mg I 5167.3 and 5173.7 Å and Ca I 6162.2 Å. The hydrogen pressure broadening parameters of these lines were adopted from Anstee & O'Mara (1995). Derived $\log g$ values are presented in Table 3. The surface gravities finally adopted in the analysis are not necessarily the straight mean of the strong-line gravities, since higher weight was put on lines with superior line-wing fits. For instance, some line wings were so wide that the continuum placement became difficult and some were blended with other strong lines. The strong Fe I lines were used with the abundance derived only from lines with low excitation energies (which were not used for the abundance analysis in Sect. 9), while for the strong Mg and Ca lines we adopted the general abundances given later in Table 6. Either, never both, of the two strong Fe I lines were used for a star. Gravities derived from assuming Fe ionisation balance are also presented in the table, but these were not used in this analysis.

5.2. Parallaxes

Trigonometric surface gravities were derived by Eq. (1).

$$\log \frac{g}{g_\odot} = 4 \log \frac{T_{\rm eff}}{T_{\rm eff\odot}} + \log \frac{\mathcal{M}}{\mathcal{M}_\odot} + 0.4(M_{\rm bol} - M_{\rm bol\odot}). \quad (1)$$

Masses were derived from the theoretical ($T_{\rm eff}$, L) isochrones of Girardi et al. (2000). One subgiant, HD 82734, appeared to be extremely luminous, why we consulted the Yale Parallax

Table 4. The sensitivities of surface gravities, $\log g$, derived from line-wings and parallaxes to a temperature change $\Delta T_{\rm eff} = +150$ K.

Star	Fe I 4383 Å	Mg I 5167 Å	Mg I 5172 Å	Fe I 5269 Å	Ca I 6162 Å	Hipparcos π
HD 400	+0.00	+0.15	+0.15			+0.05
HD 18907		+0.20	+0.20	+0.00	+0.00	+0.05
HD 130952		+0.35	+0.35	+0.10	+0.00	+0.08

Table 5. Typical sensitivities of derived abundances, [X/H], to changes in model $T_{\rm eff}$ and $\log g$.

Star	HD 400	SGB	HD 18907	SGB	HD 130952	RGB
$T_{\rm eff}/\log g$/[Fe/H]	6122/3.98/−0.24		5271/4.21/−0.46		4688/2.43/−0.28	
	$\Delta T_{\rm eff}$ +150 K	$\Delta\log g$ −0.3 dex	$\Delta T_{\rm eff}$ +150 K	$\Delta\log g$ −0.3 dex	$\Delta T_{\rm eff}$ +150 K	$\Delta\log g$ −0.3 dex
Li (Li I)	0.11	0.01	0.15	0.01	0.21	0.00
C ([C I])			−0.07	−0.16	−0.15	−0.23
C (CH)			0.11	−0.05	−0.04	−0.11
C (C_2)			0.06	−0.03	−0.03	−0.10
N (CN)			0.10	0.01	0.00	−0.03
O ([O I])			0.02	−0.14	−0.06	−0.19
Na (Na I)	0.06	0.00	0.09	−0.02	0.11	0.00
Mg (Mg I)	0.05	0.02	0.05	0.03	0.03	0.01
Mg (MgH)					−0.04	0.16
Al (Al I)	0.05	0.00	0.08	0.02	0.10	0.00
Si (Si I)	0.04	0.00	0.01	−0.01	−0.05	−0.06
Si (Si II)	−0.10	−0.10	−0.14	−0.13	−0.26	−0.16
S (S I)			−0.11	−0.09	−0.21	−0.12
K (K I)	0.13	0.08	0.14	0.12	0.19	0.08
Ca (Ca I)	0.09	0.03	0.12	0.09	0.15	0.04
Sc (Sc II)	0.03	−0.11	0.00	−0.12	−0.02	−0.13
Ti (Ti I)	0.13	0.01	0.16	0.01	0.25	0.00
Ti (Ti II)	0.03	−0.11				
V (V I)			0.19	0.00		
Cr (Cr I)	0.07	0.00	0.09	0.01	0.12	0.01
Cr (Cr II)	−0.01	−0.11	−0.04	−0.12		
Fe (Fe I)	0.08	0.01	0.08	0.00	0.07	−0.03
Fe (Fe II)	−0.01	−0.11	−0.06	−0.13	−0.15	−0.16
Co (Co I)			0.10	−0.02	0.09	−0.04
Ni (Ni I)	0.10	0.00	0.08	−0.02	0.06	−0.05
Zn (Zn I)			−0.04	−0.08	−0.12	−0.11
Y (Y II)	0.06	−0.11				
Nd (Nd II)			0.04	−0.12	0.01	−0.13
α	0.08	0.02	0.09	0.03	0.10	0.00

Catalogue (van Altena & Hoffleit 1996) and found a more reasonable parallax 5 times larger than that reported by Hipparcos (which is 9.76 mas). Bolometric corrections were calculated from Tables 3–6 in Mihalas & Binney (1981). The resulting trigonometric surface gravities are presented in Table 3.

5.3. Comparison between the methods

Allende Prieto et al. (1999) noted that large differences between $\log g$ values derived from parallaxes and LTE Fe ionisation balance do exist and can not yet be explained. The agreement between our gravities from the LTE ionisation balance method and those from parallaxes is rather poor, see Fig. 2d). The ionization balance gravities are systematically lower than the trigonometric ones for the more metal-rich stars. This trace of overionisation in Fe suggests that the derivation of $\log g$ values from the ionisation balance may be hazardous. The pattern displayed by our stars does however not match the predicted NLTE pattern or the compiled observational data of Fig. 10 in Allende Prieto et al. (1999).

In Fig. 2 also our "strong-line" surface gravities are compared with the parallax gravities. The $\log g$ values from strong Fe I lines agree better with parallax gravities than any other criterion used. For Mg there are no low excited lines in the

Table 6. Stellar atmospheric and evolutionary parameters, dynamical properties and chemical abundances. "Label" indicates whether the star is on the subgiant branch or on the red-giant branch. The velocities are relative to the LSR and the U velocity component is directed towards the galactic centre. The chemical abundances are relative to the Sun: $[X/H] = \log(N_X/N_H)_{Star} - \log(N_X/N_H)_{\odot}$ and the isotope ratio is given by number of atoms. Im parenthesis the spectral features used are given. See Sect. 9.5 for definition of the α element abundance.

HD	400	2151	6734	18907	22484	23249	24616	35410	40409	61421
Label	SGB	SGB	RGB	SGB	SGB	SGB	RGB	RGB	RGB	SGB
$T_{\rm eff}$ [K]	6122	5727	4998	5471	5965	4893	5011	4890	4755	6632
$\log g$	3.98	3.93	3.40	4.21	3.96	3.82	3.10	3.16	3.30	4.02
[M/H]	−0.24	−0.17	−0.42	−0.46	−0.06	−0.10	−0.67	−0.20	0.13	0.01
ξ_t [km s^{-1}]	1.60	2.00	1.00	1.25	2.00	2.00	1.50	1.30	1.80	1.90
M_V	3.61	3.45	3.11	3.47	3.60	3.74	2.68	1.46	2.47	2.68
Age [Gyr]	6	6	7	6	6	13	11	2	7	2
Mass [$M_{\odot}$]	1.1	1.1	1.1	1.1	1.1	1.0	1.0	1.8	1.3	1.4
U [km s^{-1}]	37	−51	60	19	12	−4	−15	−25	−62	15
V [km s^{-1}]	−4	−41	−118	−78	−10	32	−157	24	−28	−4
W [km s^{-1}]	−1	−24	46	12	−35	20	−19	15	9	−11
$V_{\rm tot}$ [km s^{-1}]	37	70	140	81	38	38	159	38	69	19
Li (Li I)	1.07	1.20	≤−0.96	−0.39	1.24			0.00	≤−1.09	≤0.25
C ([C I])		−0.14		−0.56			−0.86		−0.26	0.05
C (CH)	−0.22	−0.10	−0.40	−0.28			−0.78	−0.29	0.05	0.02
C (C_2)	−0.24	−0.23	−0.35	−0.39	−0.15	0.06	−0.72	−0.30	0.05	
$^{12}C/^{13}C$								20 ± 5	35 ± 10	
N (N I)		0.06								0.10
N (CN)	−0.41	−0.20	−0.35	−0.58			−0.86	−0.04	0.29	
O ([O I])		−0.24	−0.12	−0.01	−0.06	−0.09	−0.52	−0.06	0.07	−0.05
Na (Na I)	−0.22	−0.11	−0.20	−0.36	−0.04		−0.61	−0.24	0.22	0.07
Mg (Mg I)	−0.21	−0.03	−0.19	−0.14	−0.06		−0.26	−0.17	0.16	−0.04
Mg (MgH)			0.11			−0.43	−0.05		0.09	
Al (Al I)	−0.28	−0.07	−0.03	−0.10	−0.03			−0.09	0.31	−0.08
Si (Si I)	−0.12	−0.02	−0.12	−0.11	−0.01		−0.33	−0.06	0.40	0.08
Si (Si II)	−0.17	−0.06	−0.21	−0.33	−0.19		−0.54		0.59	0.11
S (S I)		−0.01		−0.19			−0.45		0.42	−0.01
K (K I)	0.08		−0.26	−0.32			−0.41	−0.20	0.01	0.33
Ca (Ca I)	−0.20	−0.15	−0.06	−0.10	−0.04		−0.38	−0.17	0.08	0.05
Sc (Sc II)	−0.22	−0.17	−0.20	−0.09	−0.08	0.00	−0.57	−0.04	0.25	−0.04
Ti (Ti I)	−0.07	−0.21	−0.12	−0.08			−0.37	−0.16	0.10	0.13
Ti (Ti II)	−0.34		0.06				−0.40			0.03
V (V I)			−0.22	−0.15				−0.15	0.13	
Cr (Cr I)	−0.33	−0.13	−0.36	−0.40	−0.06		−0.67	−0.22	0.08	−0.03
Cr (Cr II)	−0.26	−0.08	−0.21	−0.22			−0.57	−0.03	0.38	0.05
Fe (Fe I)	−0.24	−0.17	−0.42	−0.46	−0.06	−0.10	−0.67	−0.20	0.13	0.01
Fe (Fe II)	−0.18	−0.14	−0.36	−0.33	−0.05		−0.76	−0.06	0.40	0.10
Co (Co I)		−0.10	−0.32	−0.30			−0.62	−0.11	0.21	
Ni (Ni I)	−0.24	−0.18	−0.32	−0.35	−0.06	−0.01	−0.66	−0.15	0.22	0.00
Cu (Cu I)	−0.35			−0.20		−0.40	−0.80	−0.20	0.10	0.00
Zn (Zn I)		−0.11		−0.30		0.16	−0.49		0.45	−0.05
Y (Y II)	−0.42		−0.30							
Zr (Zr I)									0.03	
Nd (Nd II)		−0.22	−0.17	−0.17			−0.59		0.33	0.02
α	−0.15	−0.10	−0.12	−0.11	−0.04		−0.34	−0.14	0.19	0.06

observed spectral regions and the Ca line wings are not wide enough to be used for metal poor stars. The adopted surface gravities are weighted mean values of the strong-line gravities, with weights subjectively assigned depending on the fits to the line wings.

An alterative way of determining the stellar gravity would be to use the MgH lines, which are known to be gravity sensitive (Bell et al. 1985, and references therein), with the Mg abundance derived from atomic lines. We have explored whether there is a correlation between the differences

Table 6. continued.

HD	62644	82734	111028	115577	130952	142198	168723	196171	197964	199623
Label	SGB	SGB	RGB	RGB	RGB	RGB	RGB	RGB	RGB	SGB
$T_{\rm eff}$ [K]	5143	4990	4710	4754	4688	4800	4941	4697	4800	6246
$\log g$	3.42	3.11	3.10	2.75	2.43	2.91	2.95	3.00	3.25	4.27
[M/H]	−0.11	0.29	−0.06	−0.42	−0.28	−0.10	−0.14	−0.07	0.30	−0.32
ξt [km s^{-1}]	1.60	2.00	1.00	1.00	1.20	1.20	1.00	1.00	1.20	1.65
M_V	3.13	3.51	2.40	0.51	0.82	0.64	1.84	0.65	1.81	3.48
Age [Gyr]	6	4.5	13	2	6	1	4	1	1	4
Mass [$M_\odot$]	1.2	1.3	1.0	1.9	1.5	2.0	1.5	2.0	2.0	1.2
U [km s^{-1}]	56	−5	116	59	99	15	52	6	28	4
V [km s^{-1}]	−25	−4	−52	−166	−12	44	−61	15	−16	26
W [km s^{-1}]	−35	10	29	39	39	14	22	2	−4	30
$V_{\rm tot}$ [km s^{-1}]	71	12	131	180	107	49	84	17	32	40
Li (Li I)	≤−0.68	0.21		≤−1.31	≤−1.21	≤−1.06	≤−0.88		≤−0.59	1.39
C ([C I])	−0.21	0.11	−0.52	−0.62	−0.31	−0.22	−0.47	−0.15		−0.12
C (CH)	−0.27			−0.53	−0.45	−0.22				
C (C_2)	−0.22			−0.50	−0.45	−0.26	−0.43	−0.25	0.01	
$^{12}C/^{13}C$						12 ± 3	40 ± 25	18 ± 6	40 ± 15	
N (N I)										
N (CN)	−0.28			−0.40	−0.25	0.04	−0.02	0.24	0.36	
O ([O I])	−0.16	0.25	−0.09	−0.17	−0.36	−0.17	−0.32	−0.09	0.24	−0.03
Na (Na I)	−0.09	0.65	0.00	−0.32	−0.23	−0.02	−0.06	−0.06	0.36	−0.37
Mg (Mg I)	−0.04	0.23	0.04	−0.06	0.02	−0.06	−0.10	−0.06	0.25	−0.23
Mg (MgH)	−0.20			−0.13	−0.16	−0.20	−0.22	0.18	0.18	
Al (Al I)	−0.01	0.32		0.02	0.00	0.04	−0.01		0.38	−0.25
Si (Si I)	0.06	0.52	0.21	0.02	0.15	0.14	0.01	0.26	0.47	−0.23
Si (Si II)	0.23	0.76	0.25	−0.02	0.18	0.34	−0.07	0.34	0.62	
S (S I)	0.04	0.59	0.18	−0.35	0.18	0.17	0.02	0.44		−0.29
K (K I)	−0.02		−0.09		0.08	0.06	0.15		0.19	0.00
Ca (Ca I)	−0.08	0.42	0.11	−0.25	−0.01	0.00	0.01	0.00	0.28	−0.24
Sc (Sc II)	−0.11	0.45	0.08	−0.15	−0.13	0.08	−0.16	0.01	0.35	−0.29
Ti (Ti I)	−0.25	0.31	−0.05	−0.17	−0.20	0.04	−0.02	−0.24	0.25	
Ti (Ti II)										
V (V I)	−0.39	0.30	0.00	−0.24					0.35	
Cr (Cr I)	−0.17		−0.06	−0.46	−0.31		−0.14		0.18	−0.25
Cr (Cr II)	−0.04		0.12	−0.21			0.01			−0.21
Fe (Fe I)	−0.11	0.29	−0.06	−0.42	−0.28	−0.10	−0.14	−0.07	0.30	−0.32
Fe (Fe II)	−0.03	0.61	0.18	−0.26	0.10	0.20	−0.03	0.30	0.49	−0.19
Co (Co I)	−0.25		−0.10	−0.42	−0.19	0.00	−0.21		0.33	
Ni (Ni I)	−0.11	0.41	0.04	−0.34	−0.24	0.02	−0.07	−0.04	0.42	−0.36
Cu (Cu I)										
Zn (Zn I)	0.06		0.19	0.05	0.21	0.42	−0.03	0.19		
Y (Y II)										
Zr (Zr I)		0.49						−0.26	0.20	
Nd (Nd II)	−0.19		0.04	−0.33	−0.01		0.03			
α	−0.08	0.37	0.09	−0.11	−0.01	0.03	−0.03	−0.11	0.31	−0.23

Table 6. continued.

HD	207978	212487	219617
Label	SGB	SGB	SGB
$T_{\rm eff}$ [K]	6400	6202	5762
$\log g$	3.90	3.60	3.90
[M/H]	−0.47	−0.14	−1.55
$\xi_{\rm t}$ [km s^{-1}]	1.30	1.80	2.00
M_V	3.31	2.59	3.56
Age [Gyr]	4	3	13
Mass [$M_\odot$]	1.2	1.4	0.8
U [km s^{-1}]	24	60	392
V [km s^{-1}]	21	3	−326
W [km s^{-1}]	0	−3	−48
$V_{\rm tot}$ [km s^{-1}]	32	60	512
Li (Li I)	≤0.44	1.11	0.91
C ([C I])			
C (CH)	−0.64	−0.20	
C (C_2)			
$^{12}C/^{13}C$			
N (N I)			
N (CN)			
O ([O I])	−0.33	−0.21	−0.88
Na (Na I)	−0.42	−0.14	−1.64
Mg (Mg I)	−0.48	−0.22	−1.28
Mg (MgH)			
Al (Al I)	−0.50	−0.14	−1.28
Si (Si I)	−0.33	−0.14	
Si (Si II)	−0.49		
S (S I)		0.06	
K (K I)	−0.23	0.27	−1.17
Ca (Ca I)	−0.41	−0.10	−1.26
Sc (Sc II)	−0.40	−0.30	
Ti (Ti I)		−0.03	
Ti (Ti II)	−0.45	−0.31	−1.45
V (V I)			
Cr (Cr I)			
Cr (Cr II)			
Fe (Fe I)	−0.47	−0.14	−1.55
Fe (Fe II)	−0.50	−0.14	−1.55
Co (Co I)			
Ni (Ni I)	−0.51	−0.20	−1.58
Cu (Cu I)			
Zn (Zn I)			
Y (Y II)	−0.66	−0.40	−1.93
Zr (Zr I)			
Nd (Nd II)			
α	−0.41	−0.12	−1.27

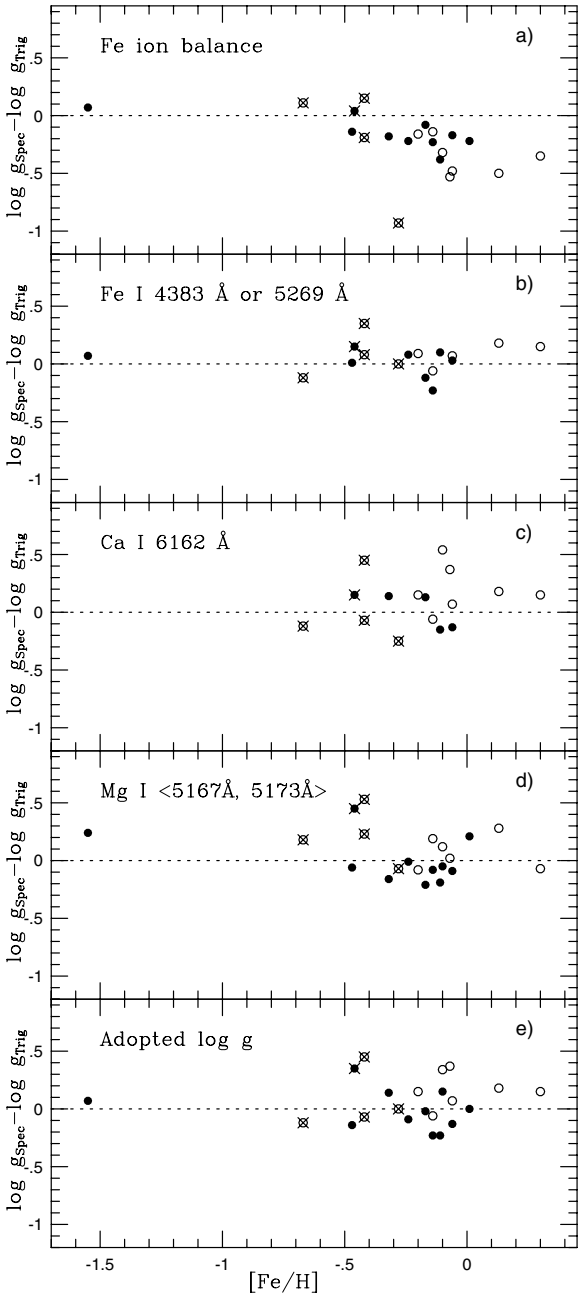

Fig. 2. Surface gravities derived by different methods minus parallax gravities. The "Fe ionization balance" panel **a**) represents results based on Fe I and Fe II lines assuming LTE ionisation balance (these were not further used in the analysis). For the strong Fe lines panel **b**), iron abundances derived from exclusively low-excitation lines were used. The Ca and Mg panels **c**) and **d**) show results from using strong lines with abundances from Table 6. Panel **e**) "Adopted log g", shows the surface gravities that were adopted in the analysis. Subgiant-branch stars are shown as solid dots and giants as open circles. Candidate thick-disk stars are identified by superposed crosses.

between the Mg abundances of Table 6 as derived from MgH and Mg I lines, respectively, and the differences between the adopted (spectroscopic) and the trigonometric gravities, and find no such correlation. That is, surface gravities from MgH would be consistent with the adopted ones at a mean, but are not good enough to improve them significantly.

6. Ages and masses

To estimate ages and stellar masses we used isochrones from Girardi et al. (2000). These authors adopted magnitudes in the V band from Kurucz (1992) model atmospheres. Interpolation in three dimensions were done with MATLAB to find age and mass for stars with metallicities between the isochrones available in the set. Figure 3 shows our programme stars with selected isochrones from Girardi et al.

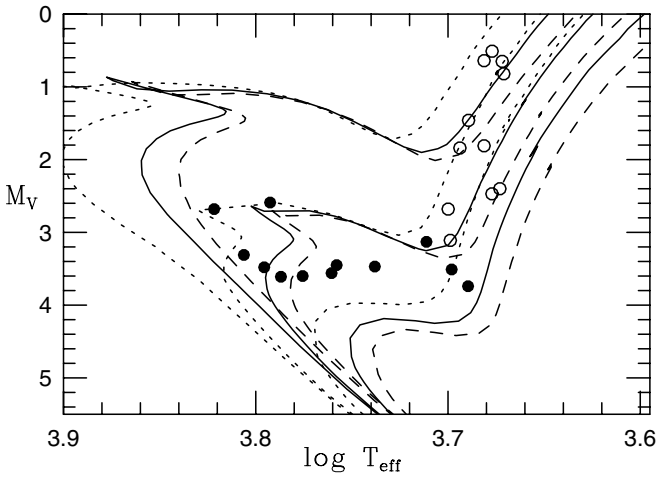

Fig. 3. The positions of our programme stars among isochrones of Girardi et al. (2000) for three metallicities and three ages. The metallicities, [Fe/H], are +0.20 (dotted lines), 0.00 (solid lines) and −0.38 (dashed lines), and the ages are, from upper left to lower right; 1.12, 3.16 and 12.6 Gyr. The subgiant stars are shown as filled circles and the giants by open circles.

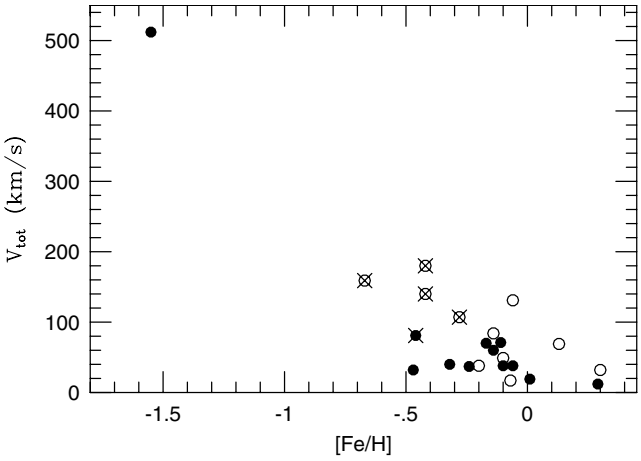

Fig. 4. [Fe/H] vs. total velocity relative to the LSR. Subgiant-branch stars are shown as solid dots and giants as open circles. Candidate thick-disk stars are identified by superposed crosses.

We compared the Girardi et. al. ages with ages derived from the isochrones by Bergbusch & VandenBerg (2001) and those by Yi et al. (2001) and found no significant differences.

The resulting masses and ages are shown in Table 6. For stars overlapping with Edvardsson et al. (1993) the ages derived agree very well. The masses and ages of the latter sample of stars were rederived by Ng & Bertelli (1998) and these also agree with our derived corresponding results.

The possibility that parallax errors will make old horisontal branch or clump stars to be mistaken for young giant stars was investigated. This is most likely to occur for approximately solar metallicity. Three stars, HD 35410, HD 115577 and HD 130952 are within one σ in M_V (using the Hipparcos standard error as σ_π) and one σ in $T_{\rm eff}$ (150 K) from the *old* clump in the isochrones corresponding to that metallicity ($Z \sim 0.019$). These three may therefore possibly be core-helium-burning clump stars.

7. Dynamical aspects

All objects have been observed by the Hipparcos satellite and have accurate proper motion and parallax data. The exception is HD 82734 as discussed in Sect. 5.2. The radial velocities were taken from the SIMBAD database, except for the radial-velocity variable HD 18907 for which a mean systemic value of $RV = +42.7\,\mathrm{km\,s^{-1}}$ was adopted (Nidever et al. 2002). Galactic U (positive in the direction of the galactic center), V (positive in the direction of the rotation of the galactic disk) and W (positive towards the north galactic pole) velocities were calculated by the formalism given by Johnson & Soderblom (1987). The total space velocity relative the local standard of rest (Dehnen & Binney 1998) is plotted versus iron abundance in Fig. 4.

In this figure and in most of the following ones we have identified five candidate thick-disk stars by overcrossed symbols. These were identified by a combination of kinematical and chemical signatures. Following Bensby et al. (2003), local stars with total space velocities relative to the local standard of rest larger than about 75 $\mathrm{km\,s^{-1}}$ have large probabilities of belonging to the "thick" component of the galactic disk. Our sample contains eight stars fulfilling this criterion. HD 219617 has a retrograde galactic orbit and a our lowest metallicity ([Fe/H] = −1.55) which puts it in the halo-star population. Four giants, HD 6734, HD 24616, HD 115577 and HD 130952, and one subgiant, HD 18907, have peculiar velocities between 80 and 180 $\mathrm{km\,s^{-1}}$, and overabundances of aluminium and α-elements as compared to the majority of disk stars of similar metallicities which is our "chemical" criterion for belonging to the thick-disk (following e.g., Fuhrmann 1998; or Feltzing et al. 2003). These five are represented by crossed symbols in the figures throughout this article. Two more giants, HD 111028 and HD 168723 have peculiar velocities of 131 and 84 $\mathrm{km\,s^{-1}}$, respectively. HD 111028 with [Fe/H] = −0.06 also shows high abundances of the α elements S, Si and Ca, but not of O and Ti. HD 168723 with [Fe/H] = −0.14 shows similar but even milder chemical peculiarities. These two giants may be metal-rich thick-disk star of the kind discovered by Feltzing et al. (2003), but we have chosen not to emphasize them further here.

The five thick-disk candidates are discussed further in Sects. 9.5 and 10.2.

8. Errors

8.1. Abundances

The chemical abundances are sensitive to the accuracy of stellar parameters, to the synthetic spectral fitting to observational data, to the atomic and molecular data and to errors caused by the assumptions of LTE and mixing-length convection in plane-parallel geometry.

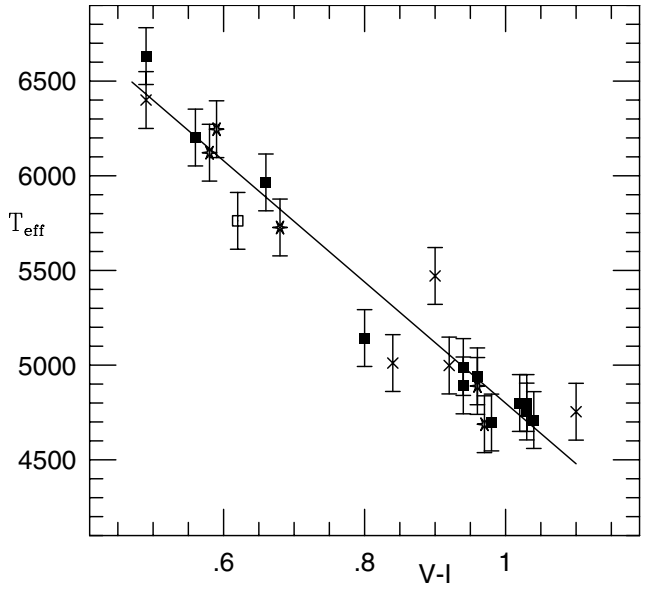

Fig. 5. $T_{\rm eff}$ versus $V-I$ colours. Open square: [Fe/H] = −1.55, crosses: −0.7 < [Fe/H] < −0.4, asterisks: −0.4 < [Fe/H] < −0.15, filled squares: [Fe/H] > −0.15. The line is fitted to the 22 stars with [Fe/H] > −1.0. These 22 scatter by 163 K around the line. The error bars represent our estimated $T_{\rm eff}$ uncertainty of 150 K.

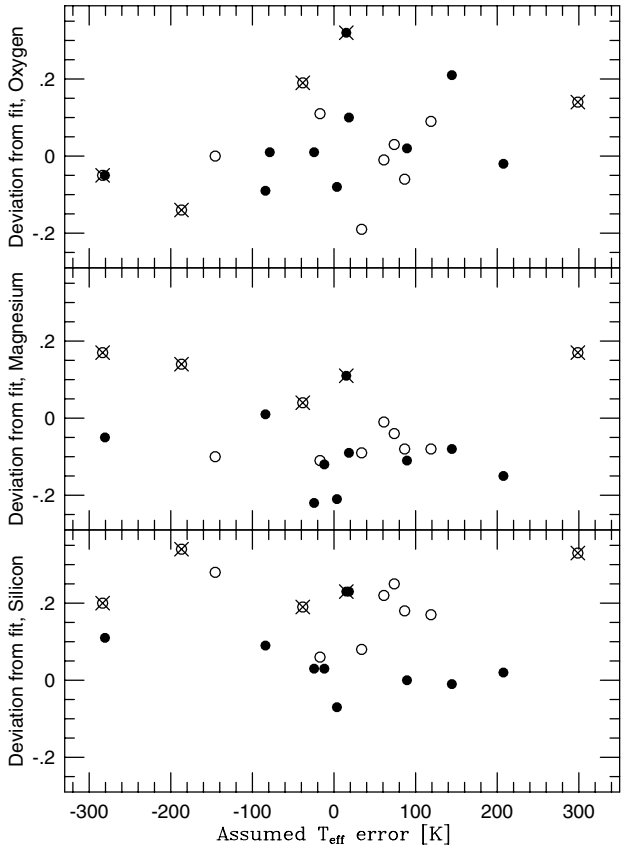

Fig. 6. Abundance deviations from fit to Edvardsson et al. (1993) data versus $T_{\rm eff}$ deviations from the line in Fig. 5, for stars with [Fe/H] > −1.0. Symbols as in Fig. 4.

8.1.1. Stellar parameters

Accurate stellar parameters are essential for getting reliable abundances. The effects of such errors on the abundances are reviewed in this section. Uncertainties in these parameters affect not only the abundances but also each other, e.g. $\log g$ depends on the adopted $T_{\rm eff}$.

Effective temperatures are often derived spectroscopically by requiring that the abundances of iron derived from Fe I lines of different excitation should not differ systematically. We note a systematic deviation for Fe abundances from low excited lines in our low $\log g$ (and low $T_{\rm eff}$) stars. This has earlier been suggested to be an NLTE effect for giant stars (Steenbock 1985) and following their results we thus choose to use high excited lines for our Fe abundances. The effective temperatures were compiled from earlier analyses, and they are therefore not very homogeneous. We estimate from earlier experience and the scatter between different investigations that our $T_{\rm eff}$ determinations are internally consistent within about 150 K. As a simple test we plot in Fig. 5 our adopted values of $T_{\rm eff}$ vs. $V-I$, as given in the Hipparcos catalogue (ESA 1997). Neither empirical nor theoretical model-atmosphere $T_{\rm eff}$ calibrations suggest any appreciable metallicity sensitivity of the $V-I$ colour at effective temperatures above 4000 K. Nevertheless, since line blanketing may affect the relation between $T_{\rm eff}$ and $V-I$, we have separated the stars into four different metallicity intervals, and plot the stars in each interval with different symbols and an error bar of ±150 K. 22 of our 23 stars have $-0.7 \leq$ [Fe/H] +0.3. The remaining star, HD 219617 (marked by an open square in Fig. 5) has [Fe/H] = −1.55 and falls below the line in the diagram. The scatter seen relative to a mean relation for the stars is consistent with an uncertainty in $T_{\rm eff}$ of about 150 K. These considerations make us adopt an uncertainty of ± 150 K for the stellar effective temperatures for the disk-metallicity stars.

The possibility that errors in the effective temperatures is an important source of the scatter in our abundance-abundance diagrams (cf. Fig. 8, Sect. 9) was empirically tested: if errors in our $T_{\rm eff}$ determinations were dominating the scatter seen in our abundance diagrams we would expect these abundance errors to be correlated with the $T_{\rm eff}$ errors. To test this we assumed the $T_{\rm eff}$ deviations from the line in Fig. 5 to be our $T_{\rm eff}$ errors. We next adopted the difference between our [X/Fe] and a linear fit of [X/Fe] vs. [Fe/H] from EAGLNT (for our 22 stars with [Fe/H] > −1.0). These differences for O I, Mg I and Si I were plotted vs. the assumed $T_{\rm eff}$ errors, but no appreciable correlations could be found, see Fig. 6. Errors in our effective temperatures are thus unlikely to dominate the scatter in the abundance diagrams.

The subgiant HD 18907 has recently been presented to show radial velocity variations (Setiawan et al. 2003). First estimates of the orbital parameters gives $P \approx 9700$ days, $a \approx 10$ AU and a mass function $f(m) = 0.018$. (Udry 2003; Setiawan 2003). Our derived primary mass is $1.1\,M_{\odot}$ and a 90° orbital inclination gives a minimum secondary mass of $0.32\,M_{\odot}$. Assuming an inclination of 60° gives a mass of $m_2 = 0.4\,M_{\odot}$ for the secondary, corresponding to a M 2 dwarf with $M_V \approx +9.9$ (Cox 1999). A parallax of 33 mas (ESA 1997) then gives a secondary flux of 0.3% of that of the primary in

the V passband and a separation on the sky of a fraction of an arcsecond. Nevertheless, without information of the orbital inclination there is still a 50% chance of a more massive secondary and there remains a possibility of errors in the equivalent widths for HD 18907 due to multiplicity. At the time of observation the primary had a radial velocity $+1.3\,\mathrm{km\,s^{-1}}$ higher than the systemic velocity and the secondary should therefore be blue-shifted by more than this amount relative to the primary ($-6\,\mathrm{km\,s^{-1}}$ for $m_2 = 0.4\,M_\odot$). We can not detect any traces of the secondary in our spectra for HD 18907.

Setiawan et al. (2004) also report that HD 62644 is a binary with $m_2 \sin i = 0.32\,M_\odot$. Also for this star we can not find any trace of a secondary spectrum, and the abundance results for the star give no reason to suspect any influence of the secondary stellar spectrum.

In Table 4 the sensitivities of $\log g$ due to uncertainties in $T_{\rm eff}$ for three typical programme stars are presented. For spectroscopic gravities, $T_{\rm eff}$ affects the fraction of neutral atoms, as well as the continuous opacity, giving generally weaker lines for higher $T_{\rm eff}$. The trigonometric surface gravity is affected through the $T_{\rm eff}$ contribution to Eq. (1) (also including a change in bolometric correction). Note that the sensitivity to $T_{\rm eff}$ errors is rather small for the parallax method. The strong-line method for determining gravities is also quite insensitive to errors in $T_{\rm eff}$ (Blackwell & Willis 1977; Edvardsson 1988) when the metal abundance is derived from weak lines with similar excitation energies. This is the case for the strong Ca and Fe lines in our sample, while for the Mg triplet lines (2.7 eV) we had to use weak lines excited to between 5 and 6 eV for the abundance determinations.

The precision of the parallax method is only weakly depending on errors in temperature and masses. The resulting mean difference between the Ca I 6162 Å gravities and the parallax gravities is +0.10 dex with a standard deviation of 0.22 dex. For the Fe I lines the corresponding numbers are +0.05 and 0.13 dex. The mean difference between the adopted gravities in the analysis and those of the parallax method is +0.06 with a scatter of 0.19 dex. We conservatively judge the mean error in the adopted surface gravities to be about 0.2 dex.

The effects on the derived abundances due to errors in $T_{\rm eff}$ and $\log g$ are shown in Table 5 for three stars with typical parameters. Our estimated error of 0.2 dex in $\log g$ would produce a typical abundance effect of ~0.05 dex and a $T_{\rm eff}$ error of 150 K changes the abundances ~0.10 dex

The microturbulence parameters were derived by requiring strong and weak Fe lines to yield equal abundances. The uncertainty in abundances due to this error source was tested for the stars in Tables 4 and 5. It was found to be significant only for the metal-rich cool giant HD 130952. For most [X/Fe] abundance ratios a change in $\xi_{\rm t}$ of $0.5\,\mathrm{km\,s^{-1}}$ caused an [X/Fe] shift of typically ~0.08 dex for this star. For the other stars an equal uncertainty in $\xi_{\rm t}$ is less important for the abundances, typically <0.05 dex.

8.1.2. Atomic data

The scatter (s.d.) in abundances derived from individual spectral lines around the mean abundance of a species is typically 0.06 dex. The formal mean error is naturally smaller, since many of the elements provided several lines for use. Tables 1 and 2 (electronically available) identifies the lines and features used for each species.

For most atomic lines the oscillator strengths were determined by fitting of solar spectra. The precision in $\log gf$ values is then dependent on the solar fits. We estimate an error < 0.05 dex from this source. Additionally, the MARCS solar model may not be ideal for finding the absolute $\log gf$ values, even if most of the errors will cancel out for stars with stellar parameters close to the solar values. For giants this cancellation may only be partial.

The lines used in the abundance analysis are mostly weak and therefore uncertainties in the pressure damping parameters have been found to have very small or no effects on the abundance results.

8.1.3. Molecules

Since the CO molecule binds a large fraction of the carbon in cool stars, the uncertainties in the C, N, O molecular equilibria are interconnected. Based on the atomic [O I] oxygen abundance, first the carbon and then the nitrogen abundance were derived. Therefore any error in the oxygen abundance will affect also the carbon and nitrogen abundances. We present here some typical abundance effects based on tests with varied abundances and model parameters.

A mild variation $\Delta\log$ O of the assumed oxygen abundance brings a typical change $\Delta\log$ C in the carbon abundances derived from CH and C_2 lines of $\Delta\log \mathrm{C} \approx +0.5\Delta\log \mathrm{O}$ with an uncertainty in the constant of 0.15 for disk stars cooler than about 5200 K. For warmer stars and our halo-metallicity star, the adopted oxygen abundances have a much smaller influence on the derived carbon abundances. For our nitrogen abundances derived from lines of CN we find correspondingly $\Delta\log \mathrm{N} \approx -\Delta\log \mathrm{C}$ since the calculated CN lines vary in proportion to the product of the total carbon and nitrogen abundances.

An effective temperature increase of 150 K, with the associated change in the atomic oxygen abundance results in carbon abundance modifications of between −0.05 to +0.10 dex. The effect for nitrogen ranges between 0.00 and +0.10 dex. Similarly, the abundance effects of a change of the surface gravities by −0.2 dex are −0.03 to −0.08 dex for C, and 0.00 to −0.03 dex for N.

8.1.4. Overionization

In Fig. 7 the empirical ionisation patterns for Si, Ti, Cr and Fe are plotted against effective temperature. Our subgiant branch stars are marked as solid dots. There are obvious trends with effective temperature for the cooler stars (open circles), which indicate systematic errors in the analysis. The coolest SGB star, HD 82734 ($T_{\rm eff}$ 4990 K), also shows strong signs of

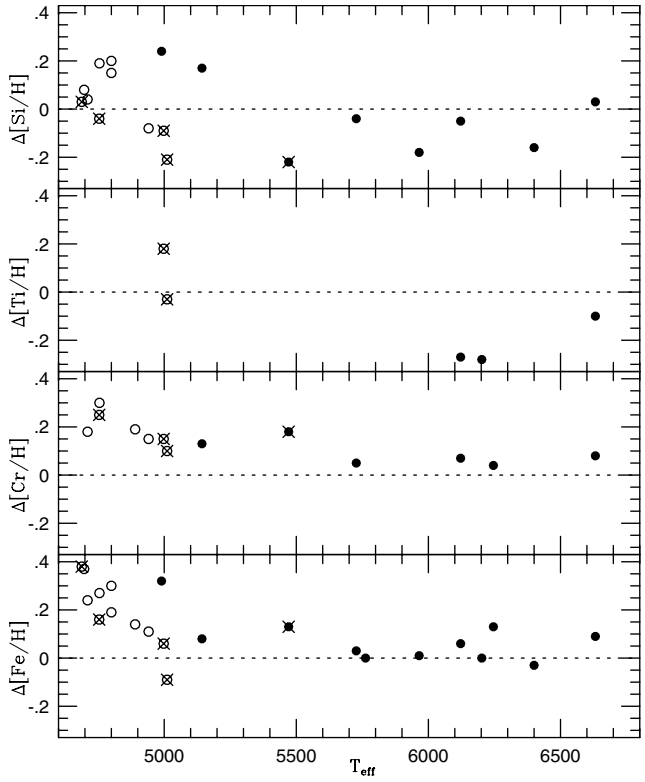

Fig. 7. Differences in abundances derived from lines of ions and neutrals. Δ[Fe/H] = [Fe/H]$_{\rm FeII}$ − [Fe/H]$_{\rm FeI}$, etc. Solid dots = SGB stars and open circles = RGB stars. Five candidate thick-disk stars are identified by crossed symbols.

overionization. This is also our most metal rich object with [Fe/H] = +0.29.

8.1.5. Summary of abundance errors

From the discussion above we find that the abundances derived are expected to be correct to about 0.2 dex for many atomic species, while the errors in carbon and in particular nitrogen abundances could be even greater. These estimates do not account for systematic errors due to departures from homogeneous (1D) stratification and other uncertainties due to convection. As has been shown in recent work on the solar CNO abundances by Allende Prieto et al. (2002), such effects may be considerable (of typically 0.2 dex). Even if one may hope that the errors in a differential study, like the present one, are smaller, and that certain abundance ratios are not very sensitive to these effects, more definitive conclusions must await detailed 3D modelling of these stars.

8.2. Uncertainties in ages and masses

The age uncertainties depend on the orientation of the isochrones. For the subgiants these are mostly about 1 Gyr, while for the giants they may be several Gyrs, due to uncertainties in the effective temperatures and the "vertical" and densely spaced isochrones. The effect on the ages of alternatively adopting isochrones from Bergbusch & VandenBerg (2001) and Yi et al. (2001) is typically about 1–2 Gyr.

A 10% error in the parallax (or 0.1 dex in $\log g$) may typically correspond to about 2 Gyrs in age uncertainty, as derived from the isochrones by VandenBerg (1983; cf. also Gustafsson 1995). Uncertainties or a cosmic spread of helium abundances of 0.05 in Y introduce further uncertainties in the ages of typically 1 Gyr (as derived from VandenBerg & Laskarides 1987), while an error in Z of 0.1 dex may lead to errors of almost as much. For stars on the sub-giant branch the effects of errors in convection theory should not be severe on the isochrones (cf. Pedersen et al. 1990). However, the use of stellar models with diffusive processes (gravitational settling and radiative accelerations) give reductions of ages of typically 0.5 Gyr (Sandage et al. 2003). We conclude that the errors in age estimates may well sum up to 3–4 Gyrs, at least for the older stars. For the RGB stars in the sample, the errors may well be larger, and in particular the error bars may include very high ages due to the degeneracy of the isochrones along the giant branch. For subgiants in the mass interval 0.8–1.5 solar masses, the age uncertainty corresponds to 0.1–0.2 solar masses in the mass estimate.

8.3. Uncertainties in the dynamical data

The Hipparcos proper motion data is mostly better than 1 and always better than 2 mas/year. The radial velocity errors are typically 1–2 km s^{-1}, except for HD 62644, for which the uncertainty is given as 5 km s^{-1}. For 15 objects, the uncertainties in the total space velocities are $\lesssim$2 km s^{-1}, 6 stars have total errors between 3 and 7 km s^{-1}, while the giant HD 115577 is uncertain by 18 and our halo subgiant HD 219617 with a retrograde galactic orbit has an uncertainty of 102 km s^{-1} in the total space velocity. These two stars have small parallaxes and therefore large relative parallax errors. In relative measure all but one star have uncertainties less than 11% of the total space velocity. HD 219617 has an error of 20%.

9. Abundance results

The resulting chemical abundances relative to the Sun are presented in Table 6 and shown in several figures below. In the following section patterns in the element ratios are discussed. Fig. 8 displays element [X/Fe] vs. [Fe/H] (derived from lines of Fe I) for several species. The abundances derived for disk stars by EAGLNT are shown as small dots for comparison.

In Figs. 8 to 17 the subgiant branch (SGB) stars are represented by solid dots, while the results for stars which have started to ascend the giant branch (RGB) are shown as open circles. Note that the RGBs sometimes display a different abundance pattern as compared to the SGBs which are the primary targets for this study. The SGB star HD 18907 and the four RGB stars HD 6734, HD 24616, HD 115577 and HD 130952 are believed to be thick-disk stars and are identified by crossed symbols in the figures. These were identified in Sect. 7 and are discussed separately in Sect. 10.2.

9.1. Lithium

Li is produced in the Big Bang and later by cosmic ray spallation and in different stellar objects (e.g., Guessoum & Kazanas 1999; Denissenkov & Weiss 2000; Ramaty et al. 2000; Travaglio et al. 2001).

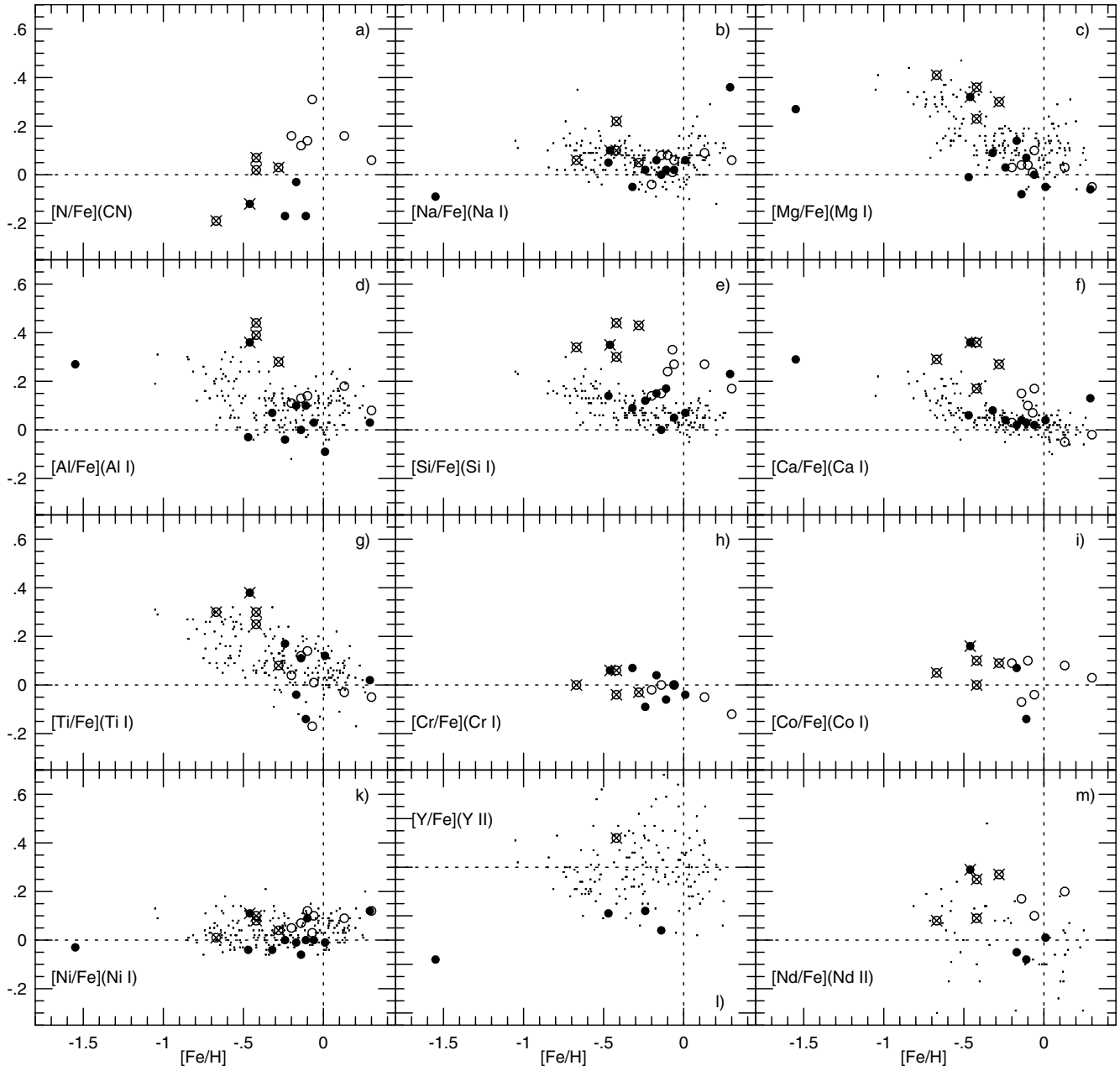

Fig. 8. Abundance-abundance diagrams for several element ratios. SGB stars are shown as solid dots while RGB stars are circles. Five candidate thick-disk stars are identified by crossed symbols. The small dots are disk star abundances from EAGLNT. The vertical scale for yttrium has been shifted by 0.3 dex.

Li is destroyed by proton capture at low stellar interior temperatures, leading to Li depletion in stellar atmospheres for which the surface matter has been subject to convective mixing with deeper regions (cf., e.g., Boesgaard 1991; Deliyannis et al. 1998). We used the 6707 Å doublet to derive the total Li abundance (^{6}Li + ^{7}Li). Li region spectra were secured for 21 stars. The line was detected in 11 stars while for 10 stars only an upper limit could be obtained. Figure 9a displays a large spread in the Li abundance diagram. Several disk stars show only low upper limits, consistent with evolutionary depletion from an initial abundance of A(Li) above 3.0. Only five disk-SGB stars show abundances above $A(\mathrm{Li}) = \log(N_{\mathrm{Li}}/N_{\mathrm{H}}) + 12 = 2.0$. These are only slightly metal deficient and seem to be depleted by about 1 dex relative to the upper envelope of A(Li) vs. [Fe/H] distribution as compiled e.g. in Fig. 6 of Ryan et al. (2001). Our halo SGB star, HD 219617 with [Fe/H] = −1.55, seems to be typical for or only slightly below the locus for non-depleted halo dwarfs.

The observed pattern also shows a T_{eff} dependent effect. Cool main sequence stars are well known to destroy Li, and the deepening surface convection zone as the stars evolve towards the giant branch will cause further Li destruction. Figure 9b shows that the stars with detected Li divides into two groups: the stars with $T_{\mathrm{eff}} < 5500$ have Li abundances $A(\mathrm{Li}) \leq 1.5$. The warmer group of stars have higher abundances but still (with the exception of HD 219617) lower than their presumed

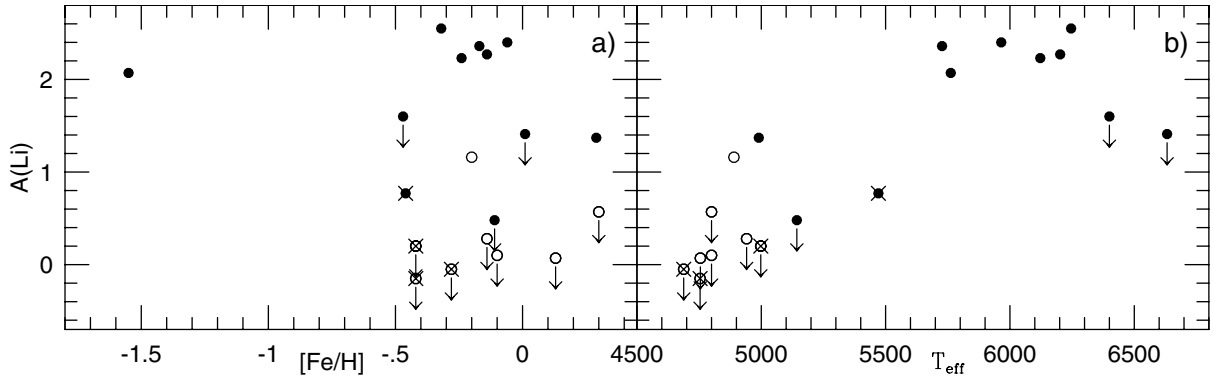

Fig. 9. Li abundances vs. metallicity and effective temperature. Symbols as in Fig. 8, and the arrows denote upper limits.

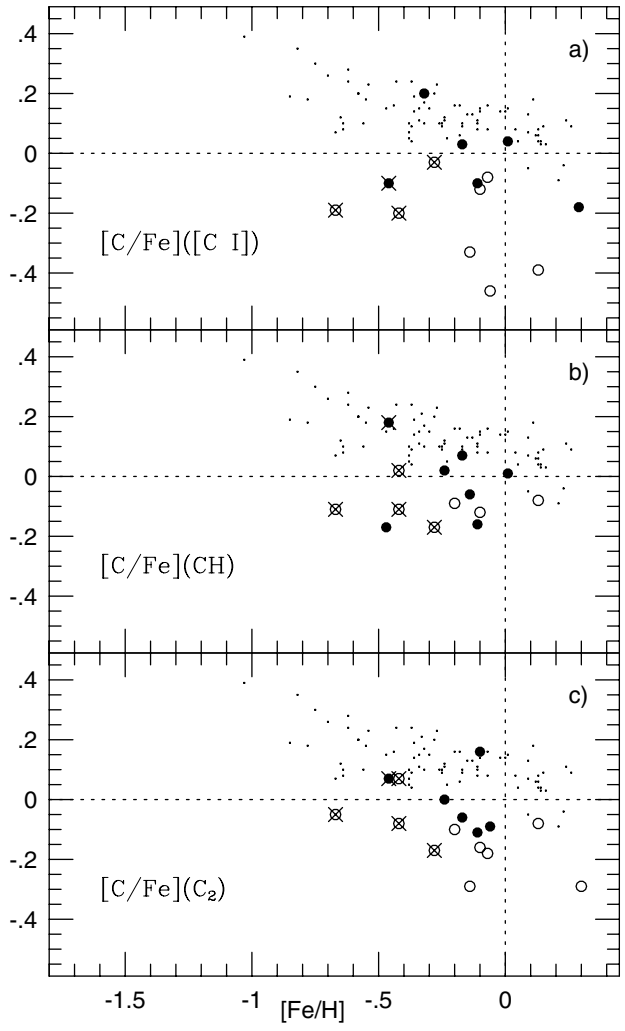

Fig. 10. [C/Fe] from [C I], CH and C_2 lines. Symbols as in Fig. 8.

primordial abundances. Our two warmest stars, the subgiants Procyon (HD 61421) and HD 207987 show no traces of the Li doublet. These may already on the main sequence have destroyed most of their Li (Boesgaard & Trippicco 1986). A plot of Li abundance vs. stellar mass, tracing main sequence $T_{\rm eff}$, does not show any evident correlation. An elaborate discussion of Li based on a large sample of subgiant stars was recently given by do Nascimento et al. (2003).

9.2. Carbon

Traces of post-main-sequence evolution could be expected for C, since this element is converted to nitrogen in the CN cycle, which is weak but existing in solar-mass dwarfs (Bahcall & Ulrich 1988), and which dominates the energy generation during the shell-hydrogen-burning phase. The effects of CN cycling is seen in the surface abundances of stars which have experienced the first dredge up.

The weak, forbidden [C I] line at 8727 Å was used for C abundance derivation for 80 F–G dwarfs by Gustafsson et al. (1999). They found a weakly increasing [C/Fe] trend with decreasing metallicity. This data are shown as small dots in Figs. 10 and 11. Here, the same forbidden line with a complementary highly excited C I line (7662 Å, in the middle of a strong telluric molecular line forest and only visible in a few of our warmest stars) could be used for half our stars. Our subgiants (solid dots) in Fig. 10a scatter more and show a somewhat lower mean value than do the dwarfs of Gustafsson et al. Only 0.03 dex of the difference can be blamed on the difference in gf values. The first line of Table 7 (in Sect. 10) compares the scatter relative to linear regressions of [C I]-line-based [C/Fe] vs. [Fe/H] for our SGBs (0.09 dex) and the dwarfs of Gustafsson et al. (0.06 dex).

The CH- and C_2-line results are shown in Figs. 10b and c. All three criteria give similar results with giants generally showing lower carbon abundances than subgiant stars at similar metallicity. Five of the subgiants seem, however, to have low carbon abundances similar to those of the least depleted giants in Fig. 11, where the straight-mean values of all carbon-abundance criteria are shown. This may possibly be an indication of deep mixing in stars which have not yet reached the giant branch. We do, however, not find any correlation between the subgiant [C/Fe] and either $M_{\rm V}$, stellar mass, or Li abundance.

$^{12}C/^{13}C$ abundance ratios could be derived for six of the giant stars with roughly solar metallicity. For the remaining stars the CN (A–X) lines were too week or not observed. In Fig. 12 the derived ratios are plotted vs. absolute magnitude. The theoretical isotopic ratios expected after the first dredge-up for stars of this metallicity and mass range are in the range 20–30 (Boothroyd & Sackmann 1999, Table 2; Girardi et al. 2000; Salaris et al. 2002). The three most luminous of

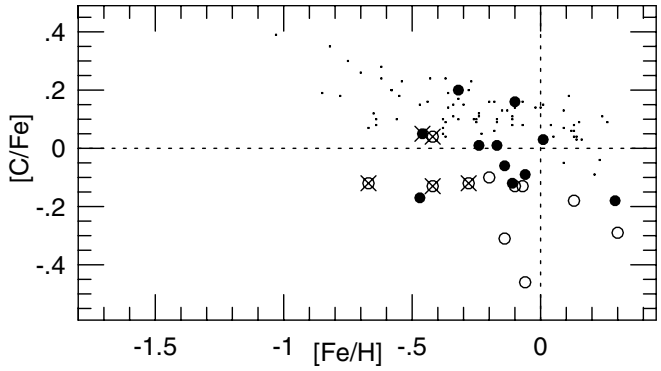

Fig. 11. Mean value of [C/Fe] from [C I], CH and C_2 lines. Symbols as in Fig. 8.

the six, $M_V < 1.5$, also show the lowest carbon isotope ratios. $^{12}C/^{13}C = 12 \pm 3$ for HD 142198 requires models with extra mixing after the first dredge-up for its explanation (see e.g., the recipe for "Cool Bottom Processing" in Table 2 of Boothroyd & Sackmann 1999).

9.3. Nitrogen

The same mechanism which depletes carbon on the giant branch would also bring fresh nitrogen to the surface. This is probably seen in Fig. 8a. Our N I line could only be measured in two stars, while the CN molecular lines could be used for half of the sample. For the subgiant HD 2151, the only star for which both criteria could be used, the N I and CN criteria give different abundances by a factor of two (0.3 dex), which calls for caution in the interpretation. One should bear in mind that the N abundances derived from CN lines are quite sensitive to the adopted carbon abundances. The linear abundance ratios N_C/N_N, using the mean values of our C and N abundance criteria, are plotted against absolute magnitude in Fig. 13. Consider separately the five crossed symbols, representing thick-disk stars, which may have had particular initial abundance ratios as discussed below in Sects. 9.5 and 10.2 and which also have lower metallicities than the other objects in this figure. This quintuplet may describe a parallel trend to the "normal" disk stars, which are discussed first: note that the six stars with $N_C/N_N \leq 2.1$ in Fig. 13 are exactly the same giants for which we could estimate $^{12}C/^{13}C$ ratios and thus verify surface abundance changes: HD 35410, HD 40409, HD 142198, HD 168723, HD 196171 and HD 197964. Boothroyd & Sackmann (1999, Table 2, BS99 below) tabulate the expected surface abundances after the 1st dredge up for stars of different masses. Their initial C/N number abundance ratio before dredge-up is however only 2.8 and their C/N given after the first dredge up for stars with masses in the range 1.3–2.3 $M_\odot$ fall between 1.2 and 0.8, respectively. This is indicated by the thick arrow. Our pre-dredge-up C/N abundance ratio (as judged from the four thin-disk subgiants in Fig. 13 is almost two times higher than that assumed by BS99. If a simple scaling of the BS99 first dredge-up C/N ratios by the initial C/N is roughly permissible, also our C/N ratios agree well with 1st dredge-up predictions, which are not noticeably affected by possible "Cool Bottom Processing".

The first dredge-up episode should show the effects of the conversion of carbon to nitrogen, while preserving the sum of the two nuclei. Figure 14 shows that [C+N/Fe], i.e. the sum of C and N normalized to the metallicity, does not scatter by more than 0.08 dex (20%) relative to a mean value of −0.06, and that there is no significant trend with luminosity.

9.4. Oxygen

ISM oxygen is supposedly produced almost exclusively in stars ending their lifes as core-collapse supernovae. The weak forbidden [O I] lines at 6300 and 6363 Å were used to estimate oxygen abundances, as well as highly excited lines in the 6150 Å region, the latter usable only for a few hot stars. The 6363 Å forbidden line is in the wings of a strong Ca I autoionisation line at 6361.8 Å, which was simulated by application of an artificially magnified radiation damping parameter, $\Gamma_{rad} = 10^{12}$ s^{-1}. In all stars except HD 400 one or both of the forbidden lines have been detected. [O/Fe] increases with decreasing [Fe/H] which is shown in Fig. 15. The subgiants display a smaller scatter around solar metallicity in Fig. 15 than do the dwarfs of EAGLNT, while they may possibly be more oxygen rich than EAGLNT around [Fe/H] ≈ –0.4.

9.5. The α elements

Mg, Si, S and Ca, our α elements, are like oxygen believed to be predominantly formed in massive stars and may therefore be expected to show similar abundance patterns. Mg is suspected to have an origin more in common with O. Titanium is sometimes expected to be formed as an iron peak element but usually shows abundance patterns similar to the α elements, cf., e.g. EAGLNT. This is also a result of this investigation, why we include it among the αs. The [Mg/H] values derived from MgH lines from 9 giants and 2 subgiants agree with the the Mg I-line results with a scatter of 0.17 dex, but they show a steeper trend with metallicity (not plotted). In the panels for [Si/Fe] and [Ca/Fe], Figs. 8e and f, several giants show abundances which are higher than those of the subgiants. The reason for this behaviour is not known, and it remains after a simple modification of e.g. the effective temperatures. We are not aware of any nucleosynthesis process which could alter these α-element abundances during early post-main-sequence evolution. We note that the subgiants also tend to follow the trends found for disk dwarfs, as we would by default expect for all our stars. It can not be excluded that the more deviating trends found for the giants disclose problems in the analysis. One possibility could be a differentially stronger overionization in Fe than in Mg, Si and Ca (cf. Fig. 7) leading to overestimated [Mg,Si,Ca/Fe]. The sulfur abundance is derived from two highly excited S I lines and [S/Fe] only shows a large scatter around a mean of +0.20 (not plotted).

Figure 16a shows [α/Fe] vs. [Fe/H], where [α/Fe] = $\frac{1}{4}$([Mg/Fe]+[Si/Fe]+[Ca/Fe]+[Ti/Fe]) as computed from the results from neutral atomic lines is defined as in EAGLNT.

Table 7. Comparison of the abundance scatter for our SGB stars with that found for disk dwarf stars by EAGLNT and Gustafsson et al. (1999). The scatter, σ, is the standard deviation from a linear fit where [X/Fe] = $a + b$ [Fe/H]. n_* = number of stars in the fit, and $n_{\rm lines}$ = maximum number of lines. For consistency, carbon abundances from molecular lines are neglected for SGB stars. Columns 5 and 6 are for SGB stars excluding HD 18907 and HD 82734, see the text for an explanation.

Abundance ratio	SGB stars					Disk dwarfs		
				Excluding 2 stars				
(species)	σ	n_*	$n_{\rm lines}$	σ	n_*	σ	n_*	$n_{\rm lines}$
[C/Fe] ([C I])	0.12	6	1	0.09	4	0.06	80	1
[O/Fe] ([O I])	0.13	10	4	0.09	8	0.07	87	4
[Na/Fe] (Na I)	0.09	10	4	0.04	8	0.07	187	2
[Mg/Fe] (Mg I)	0.10	10	6	0.07	8	0.08	178	2
[Al/Fe] (Al I)	0.12	10	2	0.07	8	0.08	184	2
[Si/Fe] (Si I)	0.10	10	9	0.05	8	0.05	189	8
[Ca/Fe] (Ca I)	0.10	10	4	0.02	8	0.05	189	4
[Ti/Fe] (Ti I)	0.14	7	6	0.13	5	0.08	182	4
[Ni/Fe] (Ni I)	0.06	11	10	0.04	9	0.05	188	20
[Nd/Fe] (Nd II)	0.09	4	2	0.03	3	0.16	52	2

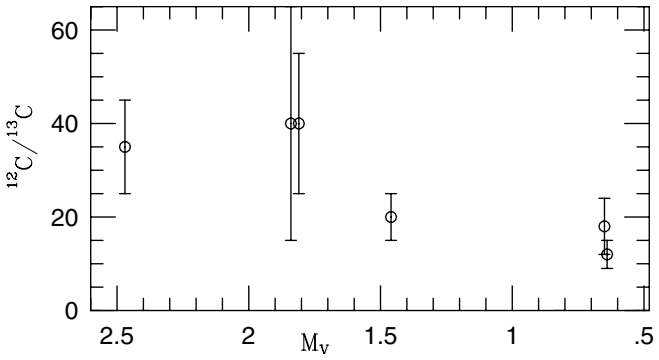

Fig. 12. $^{12}C/^{13}C$ vs. absolute magnitude Symbols as in Fig. 8.

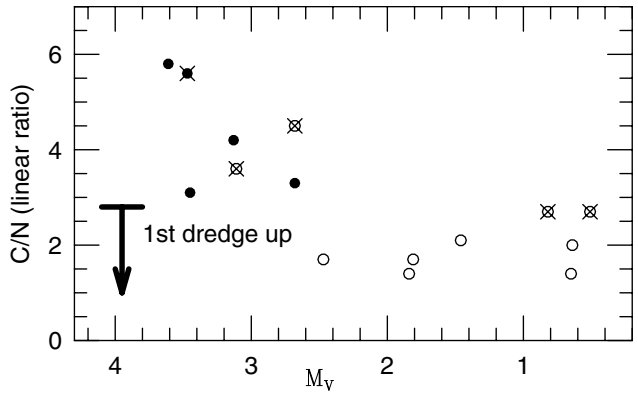

Fig. 13. N_C/N_N vs. absolute magnitude. Symbols as in Fig. 8. The arrow shows the predicted effect of the 1st dredge-up according to Boothroyd & Sackmann (1999). Its M_V is not significant since this is highly mass dependent.

Panel b) shows [α/Fe] vs. $T_{\rm eff}$. The disk-metallicity stars, excluding the group of five with crossed symbols, show no trend of [α/Fe] with effective temperature. Such trends, with different signs, do show up in individual abundance ratios relative to Fe, see e.g. Fig. 17, but each of them is based on fewer spectral lines. We consider our mean [α/Fe] ratios to be more reliable than those of individual α elements.

Most of our subgiant stars show mean α element abundances in excellent agreement with the disk dwarf stars of EAGLNT in Fig. 16a. A group of five stars, with overcrossed symbols in most of our figures and including the subgiant HD 18907, shows ratios of [Al/Fe], [Si/Fe] and [Ca/Fe], which deviate markedly from those of our other disk stars and from EAGLNT stars at similar metallicities. Also for [Mg/Fe] and [Ti/Fe] the group falls above the mean trend of the disk stars when plotted vs. [Fe/H], see Figs. 8c and g. In general this group shows abundance ratios which are similar to those of metal-poor stars, but for oxygen this is only true for the subgiant HD 18907. These "chemical" characteristics strengthen our proposal in Sect. 7 that these stars belong to the thick disk of the Galaxy. The [Fe/H] = −0.06 giant HD 111028 has a rather large total space velocity (131 km s^{-1}) and also a relatively high α-element abundance. It may therefore be a metal-rich thick-disk star of the kind recently discovered by Feltzing et al. (2003).

9.6. Sodium, aluminium and potassium

For Na and Al, Figs. 8b and d, the subgiants seem to follow the trends outlined by the disk dwarfs, while α-element-rich thick-disk-candidate stars seem to be enriched also in Al. Potassium was measured only from the outer parts of the strong wings of two resonance lines and this data is therefore uncertain and not plotted here.

9.7. Iron peak elements

The elements Cr and Ni follow Fe closely in Figs. 8h and 8k. Cobalt in Fig. 8i also follows Fe but with a slightly larger scatter. The Co I lines are weak (less than 10 mÅ in the Sun) and hyperfine structure was ignored in the analysis. [V/Fe] (not plotted) is sensitive to effective temperature and hyperfine structure, and the three thick-disk candidates with measured V I lines show ratios enhanced by about 0.25 dex while one thin-disk subgiant (HD 62644) has [V/Fe] = −0.28.

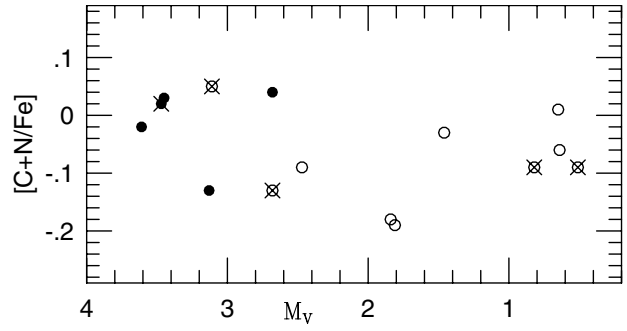

Fig. 14. The concentration of C+N nuclei relative to iron is independent of absolute magnitude as expected from the processes of CN cycling. Symbols as in Fig. 8.

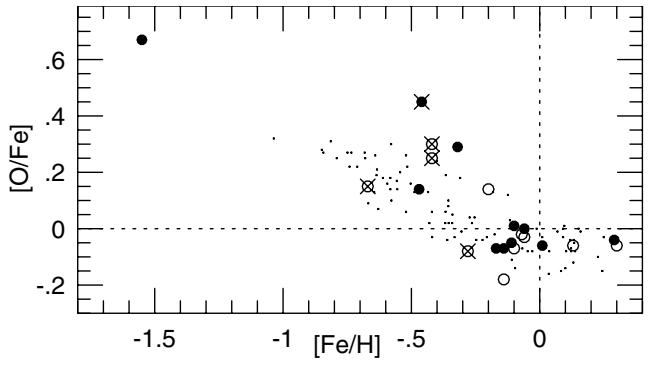

Fig. 15. [O/Fe] vs. [Fe/H]. Symbols as in Fig. 8.

The nucleosynthetic origins of copper and zinc are not well determined. [Cu/Fe] generally scatters around zero, while [Zn/Fe] displays a scatter of ±0.2 dex around +0.3. These are not plotted.

9.8. s-process elements

The elements tracing the s-process are only poorly examined in this study. One Y I line could be measured at low metallicities but was difficult to measure in the metal-rich stars. The Y abundance seems to be low in our subgiant stars, Fig. 8l, but the statistics are very poor. Nd was only measurable in disk stars and by a single Nd II line, and shows a similar pattern as the dwarfs of EAGLNT, see Fig. 8m.

10. Discussion

One key question of this study is whether abundances derived from subgiant stars are as reliable probes of the star-forming ISM as those derived from dwarfs. In Table 7 we try to quantify the scatter in the abundance ratios [X/Fe] for the SGB stars with [Fe/H] > −1.0 relative to a linear fit in the [X/Fe] vs. [Fe/H] diagram and we compare it to the corresponding quantities found for disk dwarf stars by EAGLNT and Gustafsson et al. (1999). These studies are, in terms of spectral resolution, S/N and spectral coverage roughly equivalent to the present one. When inspecting Table 7 and the diagrams we find that the scatter for the subgiants is indeed somewhat larger. Most of this scatter is, however, due to two stars which seem to depart from the others. The first one is HD 18907 at [Fe/H] = −0.46, which shows typical thick-disk characteristics and abundances very similar to our four thick-disk giants, cf. Sect. 10.2. The other deviating subgiant is HD 82734 at [Fe/H] = +0.29, which is more metal rich than any of the EAGLNT disk dwarfs that we use for comparison, and which appears particularly enriched in Na, Si, Ca and possibly Ni. If these stars are excluded one finds that the scatter is not larger than expected from known errors, and in most cases not larger than that obtained for dwarf stars in EAGLNT. In fact: for half of the abundance ratios it is smaller than for the dwarfs.

10.1. Element abundances affected by stellar evolution

One very important issue concerns the extent to which mixing of internally processed material to the surface may have affected the original abundances from the time of formation of the present subgiant stars. For lithium this is a "problem" already for main-sequence stars, and we can probably see effects of depletion in all our giants and subgiants except possibly in the subgiant HD 199623.

The next group of elements to suspect are those taking part in the CN cycle. Canonically, these effects should appear only after the first dredge-up episode, when a star has already started to climb the giant branch.

$^{12}C/^{13}C$ should show the first traces of CN cycling, but unfortunately we could not measure this ratio in any subgiant star. For the six giants where we could measure the ratio we find it to be lowered relative to the ISM as might be expected. For the giant stars we also see clear traces of carbon depletion in Fig. 11. Nine of the ten giants with nitrogen determinations show [N/Fe] > 0.0, and about 0.2 dex higher values than typical for the subgiants. This is another sign of CN cycling. Figures 13 and 14 show in an alternative way the effects of CN cycling for the giant stars.

Six of the subgiants seem not to be depleted in carbon since they fall within the scatter of the disk dwarf stars of Gustafsson et al. (1999). The five remaining subgiants with carbon abundance determinations, however, show [C/Fe] which are lower than those seen in disk dwarfs and quite similar to those of our giants at similar [Fe/H]. Only one of these, HD 62644, has a nitrogen determination which indicates a linear C/N abundance ratio of 4.2, about two times higher than typical for the CN-processed giants and typical for the four non-carbon-depleted subgiants with nitrogen determinations. A word of caution should be given regarding the nitrogen abundances mainly derived from CN molecular lines, since these abundances are very sensitive to the derived carbon abundances.

The carbon abundances derived here indicate, however, that subgiant stars may already show signs of dredge-up of CN-processed material. This should be investigated further.

For oxygen we can trace no differences in the [O/Fe] vs. [Fe/H] diagrams when we compare with results for dwarf stars in Fig. 15. Thus, no traces of other proton capture processes, e.g. ON cycling, are seen or expected.

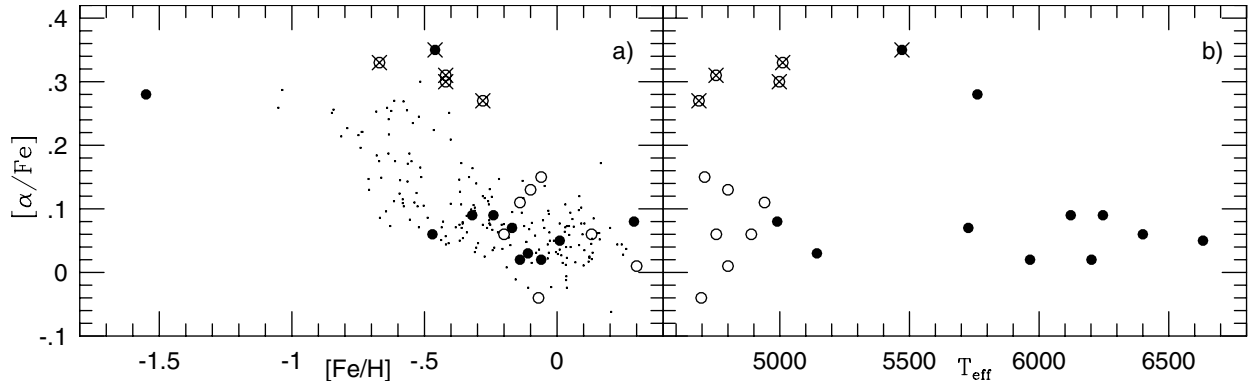

Fig. 16. [α/Fe] vs. metallicity and effective temperature. For the thin-disk stars there is no trend of [α/Fe] with effective temperature. Symbols as in Fig. 8.

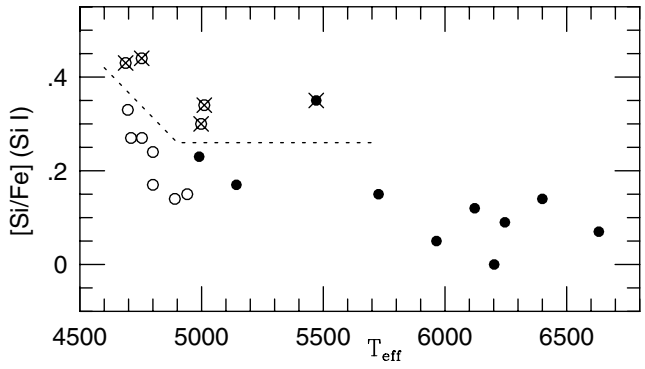

Fig. 17. Thin-disk stars, below the dotted line, show a systematic Si abundance trend with $T_{\rm eff}$. Such a trend is absent for the mean α abundance in Fig. 16b. Symbols as in Fig. 8.

10.2. The candidate thick-disk stars

In Sects. 7 and 9.5 we have identified one subgiant, HD 18907, and four giant stars HD 6734, HD 24616, HD 115577 and HD 130952, in the metallicity range $-0.67 \leq$ [Fe/H] ≤ -0.29 which show silicon, calcium and aluminium abundances which are significantly higher than those of disk dwarf stars of similar metallicities in EAGLNT. Also the magnesium and titanium abundances are higher than typical, which makes the group very "α-element" rich (Fig. 8). This derived abundance pattern is not likely to be the effect of errors in the model parameter or deviations from LTE. The abundance ratios relative to iron for this group of stars are actually quite similar to those of halo-metallicity stars.

All of these chemically deviating stars have space velocities deviating by more than 80 km s^{-1} from the LSR (Fig. 4), and, except for one giant, they have V velocities lagging behind the orbital velocity of the LSR by more than 50 km s^{-1}. These are kinematic signatures which are typical of old stellar populations.

The kinematics, aluminium and α-element enrichment suggest that the group may belong to the so-called "thick-disk" population, (Fuhrmann K. 1998; Gratton et al. 2000; Prochaska et al. 2000; Pettinger et al. 2001; Bensby et al. 2003), which has recently been proposed to contain stars with metallicities even higher than solar, see Feltzing et al. (2003). We tentatively also find overabundances in Sc, V, and Zn relative to Fe; thick-disk characteristics as proposed by Prochaska et al. The thick disk, however, is usually found to be older than about 10 Gyr (Rose & Agostinho 1993; Marques & Schuster 1994; Gratton et al.; Pettinger et al.). The estimated ages for our group of five stars are, however, not very high: 2, 6, 6, 7 and 11 Gyr. Ages derived for giants are quite sensitive to systematic errors, as stressed in Sect. 8.2 but also the subgiant, HD 18907, has an estimated age of only 6 Gyr.

11. Conclusions

11.1. The use of subgiants for studies of galactic evolution

A main result of the present study is that subgiant stars may be straightforwardly used as probes of the evolution of many chemical elements in the galactic disk. This is seen from the generally small scatter among the solid dots in Figs. 8, 15 and 16a which are quantified in Table 7. For most investigated elements, with the notable exceptions of C and N, the results for our subgiants fall within the scatter measured for disk dwarf stars. We have found indications that the surface abundances of subgiants may be affected by early dredge-up (before the canonical first dredge-up) of CN processed material. This should be further investigated by a larger sample of subgiant stars. One such sample may be the sample of 121 subgiants investigated for lithium destruction by do Nascimento et al. (2003).

The usefulness of the subgiants for studies of galactic chemical evolution is further increased by the separation of evolutionary tracks in the HR diagram for stars of different masses, and of isochrones for stars of different ages. Isochrones for subgiant stars are rather "horizontal" in the HR diagramme, which makes age determination quite insensitive to errors in effective temperatures. Stellar ages may therefore be determined from accurate absolute magnitudes or surface gravities with only rough determinations of effective temperature and of metallicity.

With parallaxes accurate to 5% one may (with luminosities estimated from apparent magnitudes) derive ages with relative accuracy better than 20% for these stars, provided that the

heavy-element abundance, Z, is known to 0.1 dex. (This also assumes that the helium abundance Y is known within 0.05 and that the convection parameter (ℓ/H_p) is known or constant with an accuracy of about 0.5, Gustafsson 1995). The age determination is not very dependent on the effective temperature as long as the star is not too close to the turn-off point or to the giant branch, i.e. as long as it is located on the almost horizontal part of the evolutionary track in the HR diagramme.

Alternatively, the ages may be estimated from the isochrones in the $T_{\rm eff}$ vs. $\log g$ diagramme, where the surface gravities are estimated spectroscopically (e.g. from the wings of strong spectral lines) or photometrically (e.g. from the Strömgren c_1 index). With an accuracy of $\log g$ of about 0.1 dex, which is difficult but obtainable today, one may then estimate ages with an accuracy of about 20% (cf. Gustafsson 1999).

So, obviously the subgiants on the horizontal part of the evolutionary track offer possibilities comparable to or even better than those of the dwarfs close to the turn-off point, exploited in their study of 189 stars by Edvardsson et al. (1993).

An important advantage is also that the subgiants are typically 1–2 mag brighter than the dwarfs, so that more distant galactic regions may be explored at a similar observational cost.

The chemically distinct group of five stars which show abundances like those of thick-disk stars, but for which we derive unexpectedly low ages, deserves a closer study of a larger sample. Is there a genuinely "young" group of α-element rich stars, or will a larger or more detailed study show that this is just an effect of small-sample statistics and uncertainties in the evolutionary tracks of giant stars?

How many suitable stars are possible to find? By cross-correlating the Hipparcos catalogue with the *uvbyβ* catalogue by Hauck & Mermilliod (1998) we find about 5×10^3 stars in the interval $2.54 < \beta < 2.79$, and with absolute magnitudes in the interval 4.3–2.0 mag, and an accuracy in distance better than 20%. The limits were set to avoid both turn-off point stars and stars on the giant branch, and the fraction of reddened main-sequence stars is judged to be minor. These stars are then generally within a distance of 250 pc, are brighter than 11.5 mag apparently and may thus be reached at high spectral resolution at telescopes of the 4-meter class. One may estimate that about 10–20 of these stars are metal poor and belong to the Halo population. Obviously, these stars together form an excellent sample for studying the the halo – thick disk – thin disk transitions in the Galaxy. In order to optimize samples for these studies rough metallicities are needed, as well as reddening data. These, as well as colour indices for estimating $T_{\rm eff}$ and $\log g$, may be found from *uvbyβ* photometry In addition to these data, kinematic data is needed. The Hipparcos catalogue gives proper motions and radial velocities are available (Barbier-Brossat & Figon 2000; Malaroda et al. 2001).

The subgiants may also be exploited in studies of the chemical evolution and in particular the thick-disk thin-disk transition, using high spectral resolution for stars at distances of up to about 1 kpc, e.g. in the Galactic Pole regions, with the VLT and other large telescopes. We estimate that one should be able to find several tens of subgiants per square degree with $V \approx 18$ mag at a distance of 1 ± 0.1 kpc from the Galactic Plane. As a preparatory to such studies one must, however, compose finding lists for survey work, e.g. using *uvby* photometry. Here, the main objective will be to separate the subgiants from dwarfs and red horizontal branch stars of similar colours. The main criterion, in addition to a colour such as $b - y$ to define the temperature interval, will be a surface gravity or luminosity criterion such as the Balmer-discontinuity-index c_1. For the task to separate the subgiants, an accuracy of 0.5 dex is needed in $\log g$, corresponding (at 5500 K) to about 0.03 mag in c_1 which is not very difficult. For this to work, however, a relatively good metallicity indicator must also be measured, such as the m_1 index. Alternatively, the f index of the narrow-band Brorfelde *gnkmf* system could be used for estimating the gravity (cf. Gustafsson & Bell 1979, and references given therein).

A third possibility is to exploit the subgiants in studies at lower spectral resolution. This possibility should be explored further, e.g. for studies towards the centre of the Galaxy.

Acknowledgements. This project was supported by the Swedish Natural Science Research Council, NFR. R. Dümmler and I. Ilyin are thanked for operating the NOT telescope and SOFIN software during the La Palma observation run and for taking additional solar spectra. J. Setiawan and S. Udry are thanked for supplying unpublished data concerning the kinematics of HD 18907 and HD 62644. Thanks are due to John Beckman for valuable comments to the manuscript, and to an anonymous referee for suggesting several improvements.
We have made use of data from the Hipparcos mission, SIMBAD, the NASA ADS and the VALD database.

References

Allende Prieto, C., García López, R., Lambert, D. L., & Gustafsson, B. 1999, ApJ 527, 879
Allende Prieto, C., Lambert, D. L., & Asplund, M. 2002, ApJ, 573, L137
van Altena, W., & Hoffleit, D. 1996, Yale Parallax Catalogue
Anstee, S. D., & O'Mara, B. J. 1995, MNRAS, 276, 859
Asplund, M., Gustafsson, B., Kiselman, D., & Eriksson, K. 1997, A&A, 318, 521
Bahcall, J. N., & Ulrich, R. K. 1988, Rev. Mod. Phys. (ISSN 0034-6861), April 1988, 60, 297
Barbier-Brossat, M., & Figon, P. 2000, A&AS, 142, 217
Barklem, P. S., & O'Mara, B. J. 1998, MNRAS, 300, 863
Bell, R. A., Edvardsson, B., & Gustafsson, B. 1985, MNRAS, 212, 497
Bensby, T., Feltzing, S., & Lundström, I. 2003, A&A, 410, 527
Bergbusch, P. A., & VandenBerg, D. A. 2001, ApJ, 556, 322
Blackwell, D. E., & Willis, R. B. 1977, MNRAS, 180, 169
Boesgaard, A. M. 1991, ApJ, 370, L95
Boesgaard, A. M., & Trippicco, M. J. 1986, ApJ, 302, L49
Boothroyd, A. I., & Sackmann, I.-J. 1999, ApJ, 510, 232
Cayrel de Strobel, G., Soubiran, C., Friel, E. D., Ralite, N., & François, P. 1997, A&AS, 124, 299
Chen, Y. Q., Nissen, P. E., Zhao, G., Zhang, H. W., & Benoni, T. 2000, A&AS, 141, 491
Costes, M., Naulin, C., & Dorthe, G. 1990, A&A, 232, 270
Cox, A. N. 1999, Allen's Astrophysical Quantities, ed. A. N. Cox (London: Athlone Press)

Dehnen, W., & Binney, J. J. 1998, MNRAS, 298, 387
Denissenkov, P. A., & Weiss, A. 2000, A&A, 358, L49
Deliyannis, C. P., Boesgaard, A. M., Stephens, A., et al. 1998, ApJ, 498, L147
Edvardsson, B. 1988, A&A, 190, 148
Edvardsson, B., Andersen, J., Gustafsson, B., et al. 1993, A&A, 275, 101 (EAGLNT)
ESA 1997, The HIPPARCOS and TYCHO Catalogues (ESA SP-1200) (Noordwijk: ESA)
Feltzing, S., Bensby, T., & Lundström, I. 2003, A&A, 397, L1
Feltzing, S., & Gustafsson, B. 1998, A&AS, 129, 237
Fuhrmann, K. 1998, A&A, 338, 161
Fuhrmann, K. 2004, Astron. Nachr., 325, 3
Girardi, L., Bressan, A., Bertelli, G., & Chiosi, C. 2000, A&AS, 141, 371
Gratton, R. G., Carretta, E., Matteucci, F., & Sneden, C. 2000, A&A, 358, 671
Guessoum, N., & Kazanas, D. 1999, ApJ, 512, 332
Gustafsson, B. 1995, IAU Symp., 166, ed. E. Hoeg, & P. K. Seidelman, 143
Gustafsson, B. 1999, in Spectrophotometric Dating of Stars and Galaxies, ed. I. Hubeny, S. Heap, & R. H. Cornett, ASP Conf. Ser., 192, 91
Gustafsson, B., & Bell, R. A. 1979, A&A, 74, 313
Gustafsson, B., Bell, R. A., Eriksson, K., & Nordlund, A. 1975, A&A, 42, 407
Gustafsson, B., Karlsson, T., Olsson, E., Edvardsson, B., & Ryde, N. 1999, A&A, 342, 426
Hauck, B., & Mermilliod, M. 1998, A&AS, 129, 431, and VizieR On-line Data Catalog: II/215
Holweger, H., & Müller, E. A. 1974, Sol. Phys., 39, 19
Johnson, D. R. H., & Soderblom, D. R. 1987, AJ, 93, 864
Jørgensen, U. G., Larsson, M., Iwamae, A., & Yu, B. 1996, A&A, 315, 204
Kurucz, R. L. 1994, in Molecules in the Stellar Environment, ed. Uffe G. Jorgensen, IAU Coll., 146, 282, also Lecture Notes in Physics, 428, 282
Kurucz, R. L. 1992, in Stellar Populations of Galaxies, ed. B. Barbuy, & A. Renzini (Dordrecht: Kluwer), 225
Kurucz, R. L., Furenlid, I., & Brault, J. 1984, Solar flux atlas from 296 to 1300 NM, National Solar Observatory Atlas, Sunspot, New Mexico: National Solar Observatory
Malaroda, S., Levato, H., & Galliani, S. 2001, Stellar Radial Velocities 1991–1998, VizieR On-line Data Catalog III/216
Marques, A., & Schuster, W. J. 1994, A&AS, 108, 341
Mihalas, D., & Binney, J. 1981, Galactic astronomy: Structure and kinematics, 2nd edition (San Francisco, CA: W. H. Freeman and Co.), 608
Moore, C. E., Minnaert, M. G. J., & Houtgast, J. 1966, The solar spectrum 2935 Å to 8770 Å, National Bureau of Standards Monograph (Washington: US Government Printing Office (USGPO))
do Nascimento, Jr. J. D., Canto Martins, B. L., Melo, C. H. F., Porto de Mello, G., & De Medeiros, J. R. 2003, A&A, 405, 723
Ng, Y. K., & Bertelli, G. 1998, A&A, 329, 943
Nidever, D. L., Marcy, G. F., Butler, R. P., Fischer, D. A., & Vogt, S. S. 2002, ApJS, 141, 503
Pedersen, B. B., VandenBerg, D. A., & Irwin, A. W. 1990, ApJ, 352, 279
Pettinger, M. M., Bernkopf, J., Fuhrmann, K., Korn, A. J., & Gehren, T. 2001, in Astronomische Gesellschaft Meet. Abstracts, 166
Piskunov, N. E., Kupka, F., Ryabchikova, T. A., Weiss, W. W., & Jeffery, C. S. 1995, A&AS, 112, 525
Plez, B. 2001, private communication
Prochaska, J. X., Naumov, S. O., Carney, B. W., McWilliam, A., & Wolfe, A. M. 2000, AJ, 120, 2513
Querci, F., Querci, M., & Kunde, V. G. 1971, A&A, 15, 256
Rose, J. A., & Agostinho, R. 1991, AJ, 101, 950
Ryan, S. G., Kajino, T., Beers, T., et al. 2001, ApJ, 549, 55
Ramaty, R., Tatischeff, V., Thibaud, J. P., Kozlovsky, B., & Mandzhavidze, N. 2000, ApJ, 534, L207
Salaris, M., Cassisi, S., & Weiss, A. 2002, PASP, 114, 375
Sandage, A., Lubin, L. M., & VandenBerg, D. A. 2003, PASP, 115, 1187
Steenbock, W. 1985, in Cool Stars with Excesses of Heavy Elements, ASSL, 114, 231
Setiawan, J., Pasquini, L., da Silva, L., von der Lühe, O., & Hatzes, A. 2003, A&A, 397, 1151
Setiawan, J. 2003, private communication
Setiawan, J., da Silva, L., Pasquini, L., et al. 2004, in Spectroscopically and Spatially Resolving the Component of Close Binary Stars, ed. R. W. Hildtich, H. Hensberge, & K. Pavlowski, ASP Conf. Ser., in press
Strömberg, G. 1930, ApJ, 71, 175
Thorén, P. 2000, A&A, 358, L21
Travaglio, C., Randich, S., Galli, D., et al. 2001, ApJ, 559, 909
Udry, S. 2003, private communication
VandenBerg, D. 1983, ApJS, 51, 29
VandenBerg, D., & Laskarides, P. G. 1987, ApJS, 64, 103
Wyller, A. A. 1966, ApJ, 143, 828
Yi, S., Demarque, P., Kim, Y.-C., et al. 2001, ApJS, 136, 417

Online Material

Table 1. Atomic data for lines of atoms and atomic ions. χ_l in Col. 3 is the excitation energy of the lower level. The Flag in Col. 5 identifies if equal to 1 that the pressure damping was taken from the quantum mechanical calculations by Barklem & O'Mara (1998) and references therein, and if equal to 0 that the classical Unsöld recipe was used with the correction factor F_6 (then given in Col. 6) to the FWHM. The last column gives the radiation damping parameter.

Species	Wavelength [Å]	χ_l [eV]	$\log gf$	Flag	F_6	$\gamma_{\rm rad}$ [s^{-1}]
Li I	6707.761	0.000	−0.009	0	2.50	3.631E+07
Li I	6707.912	0.000	−0.309	0	2.50	3.631E+07
C I	7662.431	8.771	−1.277	0	2.50	1.000E+05
C I	8727.126	1.264	−8.210	0	2.50	1.000E+05
N I	8718.835	10.336	−0.335	1	–	4.169E+08
O I	6156.755	10.741	−0.931	1	–	4.074E+07
O I	6158.187	10.741	−0.420	1	–	4.074E+07
O I	6300.304	0.000	−9.750	0	2.50	1.000E+05
O I	6363.776	0.020	−10.00	0	2.50	1.000E+05
Na I	5148.839	2.102	−2.160	0	2.00	1.000E+05
Na I	5153.402	2.104	−1.710	0	2.00	1.000E+05
Na I	6154.226	2.102	−1.625	0	2.00	7.079E+07
Na I	6160.747	2.104	−1.290	0	2.00	7.079E+07
Mg I	6318.717	5.108	−1.980	0	2.50	1.000E+05
Mg I	6319.237	5.108	−2.250	0	2.50	1.000E+05
Mg I	7691.553	5.753	−0.790	0	2.50	1.000E+05
Mg I	8712.676	5.932	−1.670	0	2.50	1.000E+05
Mg I	8717.825	5.933	−1.030	0	2.50	1.000E+05
Mg I	8736.019	5.946	−0.390	0	2.50	1.000E+05
Al I	6696.023	3.143	−1.687	0	2.50	3.020E+08
Al I	6698.673	3.143	−1.947	0	2.50	3.020E+08
Si I	6131.573	5.616	−1.850	0	1.30	1.000E+05
Si I	6131.852	5.616	−1.800	0	1.30	1.000E+05
Si I	6142.483	5.619	−1.590	0	1.30	1.000E+05
Si I	6145.016	5.616	−1.470	0	1.30	1.000E+05
Si I	6155.693	5.619	−2.440	0	1.30	1.000E+05
Si I	7688.416	6.191	−1.400	0	1.30	1.000E+05
Si I	8728.010	6.181	−0.430	1	–	1.000E+05
Si I	8742.446	5.871	−0.580	1	–	1.000E+05
Si I	8751.177	5.871	−1.850	1	–	1.000E+05
Si II	6347.109	8.121	0.257	0	2.50	1.230E+09
S I	7686.160	7.868	−1.030	0	2.50	1.000E+05
S I	8694.626	7.870	−0.080	1	–	4.169E+07
K I	7664.911	0.000	0.130	1	–	3.802E+07
K I	7698.974	0.000	−0.160	1	–	3.802E+07
Ca I	5260.387	2.521	−1.850	0	1.80	7.980E+07
Ca I	5261.704	2.521	−0.730	0	1.80	7.998E+07
Ca I	6161.297	2.523	−1.352	1	–	1.879E+07
Ca I	6166.439	2.521	−1.244	1	–	1.858E+07
Sc II	6300.698	1.507	−2.087	0	2.50	2.312E+08
Sc II	6320.851	1.500	−1.919	0	2.50	2.301E+08
Ti I	5247.289	2.103	−0.827	1	–	6.012E+07
Ti I	5295.775	1.067	−1.733	1	–	4.864E+06
Ti I	6303.756	1.443	−1.666	1	–	1.750E+08
Ti I	6312.236	1.460	−1.552	1	–	1.698E+08
Ti I	8675.372	1.067	−1.669	1	–	7.096E+06
Ti I	8682.980	1.053	−1.941	1	–	7.534E+06
Ti II	4395.850	1.243	−1.970	0	2.50	2.958E+08
Ti II	4398.271	1.224	−2.780	0	2.50	2.958E+08
Ti II	4409.516	1.231	−2.570	0	2.50	2.958E+08
Ti II	4417.719	1.165	−1.230	0	2.50	1.679E+08
Ti II	4418.330	1.237	−1.990	0	2.50	2.958E+08
Ti II	5185.913	1.893	−1.440	0	2.50	2.328E+08
V I	6274.649	0.267	−1.670	1	–	3.097E+06
V I	6285.150	0.275	−1.660	1	–	2.917E+06

Table 1. continued.

Species	Wavelength [Å]	χ_1 [eV]	$\log gf$	Flag	F_6	$\gamma_{\rm rad}$ [s^{-1}]
V I	6296.487	0.301	−1.700	1	–	3.069E+06
Cr I	5177.418	3.428	−0.570	0	2.50	7.907E+07
Cr I	5243.364	3.395	−0.667	1	–	8.091E+07
Cr I	5265.157	3.428	−0.529	0	2.50	8.091E+07
Cr I	5272.007	3.449	−0.572	0	2.50	2.518E+08
Cr II	5246.768	3.714	−2.516	0	2.50	2.312E+08
Cr II	5279.876	4.073	−2.100	0	2.50	2.553E+08
Fe I	4388.407	3.602	−0.682	1	–	8.790E+07
Fe I	4389.245	0.052	−4.533	1	–	3.381E+04
Fe I	5159.058	4.280	−0.820	1	–	1.067E+08
Fe I	5242.491	3.634	−1.167	0	1.40	5.754E+07
Fe I	5247.050	0.087	−4.946	1	–	7.834E+03
Fe I	5250.646	2.198	−2.081	1	–	1.698E+08
Fe I	5253.462	3.283	−1.573	1	–	7.499E+07
Fe I	5263.306	3.266	−0.879	1	–	7.516E+07
Fe I	5263.865	3.573	−2.135	1	–	1.641E+07
Fe I	5288.525	3.694	−1.708	0	1.40	5.957E+07
Fe I	5293.959	4.143	−1.820	0	1.40	1.660E+08
Fe I	5294.548	3.640	−2.710	0	1.40	1.340E+08
Fe I	5295.312	4.415	−1.590	1	–	1.837E+08
Fe I	6136.995	2.198	−3.050	1	–	1.648E+08
Fe I	6139.648	2.588	−4.500	1	–	1.611E+08
Fe I	6145.420	3.368	−3.600	1	–	1.175E+08
Fe I	6151.618	2.176	−3.369	1	–	1.549E+08
Fe I	6157.728	4.076	−1.260	1	–	5.023E+07
Fe I	6159.378	4.607	−1.888	1	–	1.919E+08
Fe I	6165.360	4.143	−1.540	1	–	8.770E+07
Fe I	6173.336	2.223	−3.002	1	–	1.671E+08
Fe I	6180.204	2.727	−2.686	0	1.40	1.469E+08
Fe I	6187.398	2.832	−4.165	1	–	1.449E+08
Fe I	6270.225	2.858	−2.464	0	1.40	1.449E+08
Fe I	6271.279	3.332	−2.703	0	1.40	1.186E+08
Fe I	6290.545	2.588	−4.330	1	–	1.698E+08
Fe I	6290.969	4.733	−0.568	1	–	2.286E+08
Fe I	6293.923	4.835	−1.605	1	–	1.750E+08
Fe I	6301.501	3.654	−0.718	1	–	8.054E+07
Fe I	6302.494	3.686	−1.203	1	–	8.110E+07
Fe I	6311.500	2.831	−3.141	0	1.40	1.449E+08
Fe I	6315.812	4.076	−1.610	0	1.40	5.957E+07
Fe I	6322.686	2.588	−2.356	1	–	1.021E+08
Fe I	6330.850	4.733	−1.200	0	1.40	2.382E+08
Fe I	6335.331	2.198	−2.177	0	1.40	1.660E+08
Fe I	6336.824	3.686	−0.856	0	1.40	8.110E+07
Fe I	6338.877	4.795	−0.860	0	1.40	2.275E+08
Fe I	6344.149	2.433	−2.823	0	1.40	8.710E+07
Fe I	6355.029	2.845	−2.300	0	1.40	1.449E+08
Fe I	6358.698	0.859	−4.468	0	1.40	1.000E+05
Fe I	6364.366	4.795	−1.240	0	1.40	2.317E+08
Fe I	6364.701	4.584	−1.969	0	1.40	1.169E+08
Fe I	6677.987	2.692	−1.418	0	1.40	1.021E+08
Fe I	6703.567	2.758	−2.990	0	1.40	1.030E+08
Fe I	6704.481	4.217	−2.660	0	1.40	1.000E+05
Fe I	6705.101	4.607	−1.096	1	–	2.270E+08
Fe I	6710.319	1.485	−4.780	0	1.40	1.660E+07
Fe I	6713.046	4.607	−1.548	0	1.40	2.350E+08
Fe I	6713.745	4.795	−1.450	0	1.40	2.355E+08
Fe I	6716.237	4.580	−1.800	0	1.40	5.957E+07
Fe I	6725.357	4.103	−2.200	1	–	2.089E+08

Table 1. continued.

Species	Wavelength [Å]	χ_1 [eV]	$\log gf$	Flag	F_6	$\gamma_{\rm rad}$ [s^{-1}]
Fe I	6726.661	4.607	−1.029	1	–	2.286E+08
Fe I	7664.293	2.990	−1.533	0	1.40	1.030E+08
Fe I	7719.038	5.033	−1.071	1	–	6.353E+08
Fe I	7723.208	2.279	−3.437	0	1.40	7.047E+06
Fe I	7745.500	5.086	−1.189	1	–	6.368E+08
Fe I	7748.270	2.949	−1.751	0	1.40	1.021E+08
Fe I	8674.746	2.831	−1.800	0	1.40	7.691E+06
Fe I	8680.789	4.186	−2.813	0	1.40	6.683E+07
Fe I	8698.707	2.990	−3.383	1	–	9.683E+07
Fe I	8699.454	4.955	−0.540	0	1.40	4.786E+08
Fe I	8710.392	4.913	−0.496	1	–	5.572E+08
Fe I	8729.148	3.415	−2.854	1	–	1.449E+08
Fe I	8757.188	2.845	−2.059	0	1.40	7.691E+06
Fe II	4416.830	2.778	−2.800	0	2.50	4.112E+08
Fe II	5264.812	3.230	−3.190	0	2.50	4.112E+08
Fe II	5284.109	2.891	−3.290	0	2.50	3.428E+08
Fe II	6149.258	3.889	−2.820	0	2.50	3.388E+08
Fe II	7711.723	3.903	−2.650	0	2.50	4.121E+08
Co I	5254.647	3.971	−0.249	1	–	1.091E+08
Co I	7712.665	2.542	−1.670	1	–	6.457E+06
Ni I	5157.976	3.606	−1.590	1	–	1.239E+08
Ni I	6175.360	4.089	−0.572	1	–	2.328E+08
Ni I	6177.236	1.826	−3.609	0	2.50	4.305E+07
Ni I	6186.709	4.105	−0.980	1	–	2.056E+08
Ni I	6327.593	1.676	−3.150	0	2.50	7.161E+07
Ni I	6360.808	4.167	−1.179	1	–	2.153E+08
Ni I	6366.476	4.167	−1.004	1	–	2.178E+08
Ni I	6370.341	3.542	−1.940	1	–	1.479E+08
Ni I	6378.247	4.154	−0.830	1	–	2.075E+08
Ni I	7748.891	3.706	−0.343	1	–	9.528E+07
Cu I	5105.545	1.39	−1.738	1	–	1.000E+05
Zn I	6362.338	5.796	0.100	1	–	1.000E+05
Y II	4398.013	0.130	−1.000	0	2.50	1.000E+05
Zr I	6140.460	0.519	−1.410	1	–	1.000E+05
Nd II	5249.576	0.980	−5.210	1	–	1.000E+05
Nd II	5255.506	0.200	−0.740	1	–	1.000E+05

Table 2. Molecular data. χ_l in Col. 3 is the excitation energy of the lower level.

Species/band	Wavelength [Å]	χ_l [eV]	$\log gf$
CH A-X	4186.621	0.706	−1.381
CH A-X	4186.627	0.705	−1.395
CH A-X	4204.743	0.519	−1.440
CH A-X	4204.780	0.520	−1.421
CH A-X	4207.408	0.955	−1.480
CH A-X	4207.408	0.955	−1.466
CH A-X	4210.943	0.463	−1.457
CH A-X	4210.995	0.463	−1.437
CH A-X	4211.895	0.895	−1.495
CH A-X	4211.895	0.895	−1.478
CH A-X	4212.610	0.464	−1.437
CH A-X	4212.672	0.464	−1.457
CH A-X	4213.839	0.897	−1.478
CH A-X	4213.909	0.897	−1.495
CH A-X	4216.599	0.838	−1.510
CH A-X	4216.599	0.839	−1.492
CH A-X	4217.194	0.410	−1.476
CH A-X	4217.267	0.410	−1.454
CH A-X	4218.392	0.840	−1.492
CH A-X	4218.711	0.411	−1.454
CH A-X	4218.746	0.411	−1.476
CH A-X	4288.726	0.641	−1.195
CH A-X	4288.742	0.641	−1.178
CH A-X	4293.017	0.580	−1.195
CH A-X	4293.089	0.519	−1.234
CH A-X	4293.124	0.580	−1.214
CH A-X	4293.135	0.520	−1.214
CH A-X	4303.914	0.269	−1.340
CH A-X	4303.936	0.002	−1.948
CH A-X	4303.940	0.002	−1.948
CH A-X	4306.143	0.189	−1.410
CH A-X	4306.701	0.190	−1.451
CH A-X	4306.814	0.557	−1.440
CH A-X	4306.859	0.190	−1.410
CH A-X	4310.095	0.096	−1.554
CH A-X	4310.117	0.096	−1.614
CH A-X	4311.000	0.072	−1.690
CH A-X	4311.158	0.072	−1.618
CH A-X	4311.430	0.072	−1.618
CH A-X	4311.510	0.051	−1.785
CH A-X	4311.737	0.051	−1.785
CH A-X	4312.092	0.051	−1.696
CH A-X	4312.161	0.033	−1.911
CH A-X	4313.593	0.020	−1.939
CH A-X	4313.664	0.020	−1.939
C_2 A-X	5086.248	0.331	0.089
C_2 A-X	5086.398	0.331	0.077
C_2 A-X	5103.675	0.253	0.010
C_2 A-X	5103.740	0.253	−0.004
C_2 A-X	5111.630	0.219	−0.035
C_2 A-X	5111.761	0.219	−0.051
C_2 A-X	5114.190	0.209	−0.051
C_2 A-X	5114.282	0.209	−0.068
C_2 A-X	5155.463	0.277	0.020
C_2 A-X	5155.490	0.277	0.006
C_2 A-X	5155.581	0.277	−0.008
C_2 A-X	5159.411	0.230	−0.039

Table 2. continued.

Species/band	Wavelength [Å]	χ_l [eV]	$\log gf$
C_2 A-X	5159.452	0.230	−0.055
C_2 A-X	5159.539	0.230	−0.071
C_2 A-X	5160.220	0.219	−0.055
C_2 A-X	5160.305	0.219	−0.072
C_2 A-X	5160.337	0.219	−0.088
C_2 A-X	5164.815	0.140	−0.258
C_2 A-X	5164.901	0.140	−0.284
C_2 A-X	5164.921	0.133	−0.258
C_2 A-X	5164.981	0.109	−0.376
C_2 A-X	5165.001	0.133	−0.285
C_2 A-X	5165.028	0.126	−0.284
C_2 A-X	5165.054	0.115	−0.343
C_2 A-X	5165.060	0.133	−0.312
C_2 A-X	5165.080	0.120	−0.313
C_2 A-X	5165.104	0.126	−0.313
C_2 A-X	5165.130	0.115	−0.377
C_2 A-X	5165.157	0.120	−0.344
C_2 A-X	5165.191	0.126	−0.343
C_2 A-X	5165.218	0.120	−0.375
CN B-X	4182.209	0.392	−1.287
CN B-X	4182.255	0.392	−1.304
CN B-X	4194.222	0.825	−0.886
CN B-X	4194.291	0.825	−0.898
CN B-X	4195.903	0.745	−0.949
CN B-X	4195.963	0.745	−0.963
CN B-X	4196.857	0.677	−1.022
CN B-X	4196.863	0.591	−1.172
CN B-X	4196.898	0.591	−1.195
CN B-X	4196.906	0.677	−1.038
CN B-X	4196.960	0.664	−1.038
CN B-X	4196.964	0.600	−1.150
CN B-X	4197.001	0.600	−1.172
CN B-X	4197.008	0.664	−1.055
CN B-X	4197.033	0.652	−1.055
CN B-X	4197.037	0.609	−1.129
CN B-X	4197.075	0.609	−1.150
CN B-X	4197.078	0.641	−1.072
CN B-X	4197.079	0.652	−1.072
CN B-X	4197.080	0.619	−1.110
CN B-X	4197.093	0.630	−1.091
CN B-X	4197.120	0.619	−1.129
CN B-X	4197.122	0.641	−1.091
CN B-X	4197.136	0.630	−1.110
CN B-X	4214.225	0.513	−1.166
CN B-X	4214.281	0.513	−1.180
CN B-X	4214.537	0.498	−1.180
CN B-X	4214.592	0.498	−1.193
CN B-X	4214.818	0.483	−1.193
CN A-X	7922.730	0.152	−1.963
CN A-X	7922.943	0.064	−1.910
CN A-X	7927.914	0.072	−1.879
CN A-X	7927.952	0.164	−1.944
CN A-X	7929.771	0.049	−1.945
CN A-X	7930.250	0.037	−2.411
CN A-X	7933.449	0.177	−1.927
CN A-X	7938.635	0.089	−1.821
CN A-X	7939.222	0.190	−1.910
CN A-X	7948.773	0.190	−1.886

Table 2. continued.

Species/band	Wavelength [Å]	χ_1 [eV]	$\log gf$
CN A-X	7948.812	0.037	−2.402
CN A-X	7950.414	0.108	−1.771
CN A-X	7951.604	0.217	−1.878
CN A-X	7951.723	0.089	−1.796
CN A-X	7954.096	0.043	−2.355
CN A-X	7954.584	0.203	−1.871
CN A-X	7956.706	0.118	−1.747
CN A-X	7957.013	0.098	−1.771
CN A-X	7959.694	0.049	−2.313
CN A-X	7967.087	0.232	−1.843
CN A-X	7973.781	0.247	−1.829
CN A-X	7977.224	0.152	−1.684
CN A-X	7978.359	0.072	−2.204
CN A-X	7978.511	0.089	−2.153
CN A-X	7980.772	0.262	−1.816
CN A-X	7981.155	0.140	−1.684
CN A-X	7984.619	0.164	−1.665
CN A-X	7985.201	0.080	−2.172
CN A-X	7987.939	0.152	−1.665
CN A-X	7988.062	0.278	−1.804
CN A-X	7995.572	0.311	−1.797
CN A-X	7995.650	0.294	−1.792
CN A-X	8010.088	0.190	−1.613
^{13}CN A-X	7931.457	0.058	−2.174
^{13}CN A-X	7934.198	0.066	−2.144
^{13}CN A-X	7940.078	0.032	−2.249
^{13}CN A-X	7940.418	0.083	−2.089
^{13}CN A-X	7948.226	0.066	−2.098
^{13}CN A-X	7952.555	0.038	−2.018
^{13}CN A-X	7955.921	0.121	−1.997
^{13}CN A-X	7956.027	0.010	−2.285
^{13}CN A-X	7957.555	0.014	−2.220
^{13}CN A-X	7960.441	0.132	−1.977
^{13}CN A-X	7964.022	0.027	−2.062
^{13}CN A-X	7966.780	0.032	−2.019
^{13}CN A-X	7966.863	0.027	−2.458
^{13}CN A-X	7967.385	0.121	−1.966
^{13}CN A-X	7975.401	0.074	−1.846
^{13}CN A-X	7975.567	0.167	−1.922
^{13}CN A-X	7976.024	0.143	−1.930
^{13}CN A-X	7976.821	0.051	−1.908
^{13}CN A-X	7985.794	0.167	−1.897
^{13}CN A-X	7986.283	0.092	−1.791
^{13}CN A-X	7989.503	0.074	−1.818
^{13}CN A-X	7991.111	0.179	−1.881
^{13}CN A-X	7991.111	0.051	−2.280
^{13}CN A-X	7993.100	0.206	−1.873
^{13}CN A-X	7998.205	0.111	−1.743
^{13}CN A-X	7999.421	0.219	−1.858
^{13}CN A-X	7999.421	0.092	−1.767
^{13}CN A-X	8004.554	0.121	−1.721
^{13}CN A-X	8004.781	0.066	−2.210
^{13}CN A-X	8004.728	0.101	−1.743
^{13}CN A-X	8006.060	0.234	−1.844
^{13}CN A-X	8010.458	0.111	−1.721
^{13}CN A-X	8011.163	0.132	−1.700

Table 2. continued.

Species/band	Wavelength [Å]	χ_1 [eV]	$\log gf$
^{13}CN A-X	8015.166	0.234	−1.824
^{13}CN A-X	8016.419	0.121	−1.700
MgH A-X	5144.030	0.284	0.127
MgH A-X	5149.810	0.264	0.485
MgH A-X	5151.164	0.227	−0.090
MgH A-X	5151.180	0.672	−0.008
MgH A-X	5153.670	0.238	0.485
MgH A-X	5157.000	0.213	0.461
MgH A-X	5165.945	0.147	0.382
MgH A-X	5176.800	0.064	0.155
MgH A-X	5178.434	0.487	0.003
MgH A-X	5178.480	0.051	0.103
MgH A-X	5180.590	0.040	0.103
MgH A-X	5190.550	0.587	0.345